

A detailed view on the rebar-to-concrete interaction based on refined measurement techniques

Raffaele Cantone^{*}, Miguel Fernández Ruiz, Aurelio Muttoni

École Polytechnique Fédérale de Lausanne, ENAC, CH-1015 Lausanne, Switzerland

ARTICLE INFO

Keywords:

Rebar-to-concrete interaction
Bond
Stress concentration
Fibre optic strain sensors
Shear failure
Dowel action
Cyclic response of concrete

ABSTRACT

Simplified assumptions have traditionally been made on the rebar-to-concrete interaction in structural concrete to calculate the stress state in rebars. Such assumptions typically consider a uniform stress state in the reinforcement at a given cross section, neglecting compatibility of deformations due to bending of the bar. Such simplifications are fully justified due to the relatively ductile behaviour of the reinforcement. When the ductility is however not sufficient, as for instance in case of fatigue effects in metallic reinforcement or in case of brittle non-metallic reinforcement, corrections have in many cases been proposed on an empirical base. A step forward in the understanding of these latter cases requires a detailed insight of the mechanisms of transfer of forces and the actual strain state of embedded reinforcement, which has not been possible in the past due to limitations in measurement systems.

Within this frame, this paper revisits the results of classical tests on bond, tension and bending with the insight provided by detailed measurements on the rebars. On the basis of Fibre-Optic Measurements (FOM) performed along the length of a bar and at different locations, the results show the complexity of the actual interactions between the reinforcement and the surrounding concrete as well as the influence of compatibility of deformations on their response. The results provide a new perspective on the rebar-to-concrete interaction and show its implications on a series of phenomena related to brittle failure modes.

1. Introduction

Structural concrete is a highly complex composite material in which the interaction between the concrete matrix and the embedded reinforcement bars has traditionally been approached for design purposes with simplified methods. In most cases, assuming that the reinforcement presents a large deformation capacity and toughness, several phenomena associated with compatibility of deformations (due to shearing or bending of the bars) can be neglected, as well as those related to stress concentrations resulting from the mechanical engagement of the ribs of the bars.

Some instances of phenomena traditionally neglected, such as the consideration of a non-uniform profile of stresses in the longitudinal reinforcement due to the curvature of plane sections in bending (a phenomenon already acknowledged by Ritter in 1899, [1], see Fig. 1a) or dowelling of reinforcement in the shear verification of beams and slabs, Fig. 1b. With respect to the steel-to-concrete interaction [2,3], the bond stress is usually considered as distributed over the nominal interface surface, but shows in fact high concentrations at the ribs (Fig. 1c),

where the influence of transverse strains in the bar and the presence of local punching cracks plays a major role [4,5].

These simplifications consider in fact a uniform stress state at each section of a rebar. Such consideration is reasonable for most design purposes but a fundamental understanding of the actual response of concrete is required to clarify its limits of applicability and to yield to more comprehensive design approaches. This is particularly relevant for instance with respect to brittle reinforcement response, as for non-metallic reinforcement [6]. Also, such considerations might play a governing role for some phenomena where failure is associated to stress concentrations even at serviceability limit state, as for fatigue issues [7,8]. For the latter, the actual strains might notably differ from the calculated values if compatibility of deformations [7] and stress concentrations are neglected.

The lack of detailed experimental data on the rebar-to-concrete interaction has been associated to the limitations of conventional measurement devices. Typically, measurements have been performed so far by recording displacements (by means for instance of Linear Variable Displacement Transformers, LVDTs) or by gluing strain gages on the concrete or rebar (the latter severely influencing bond properties if

^{*} Corresponding author.

E-mail address: raffaele.cantone@epfl.ch (R. Cantone).

Notation		
A	gross cross-sectional area	elastic-cracked analysis
A_s	reinforcement cross-sectional area	σ_{sa} steel stress at crack location after loading
$A_{s,eff}$	effective reinforcement cross-sectional area	σ_{si} steel stress at crack location after unloading
c_{nom}	nominal concrete cover	σ_{per} residual stress
χ_s	local curvature of the rebar	σ_{max} maximum steel stress
d_{nom}	nominal effective depth of the beam	σ_{min} minimum steel stress
δ	relative bar-concrete slip	$\bar{\sigma}_c$ concrete stress after unloading
$\Delta\sigma$	stress variation	σ_c concrete stress
$\Delta\sigma_s$	stress variation in the reinforcement	τ bond stress
Δh_v	transversal shear displacement of reinforcement	τ_b rigid-plastic bond stress
ϵ_s	bar strain	τ_a rigid-plastic bond stress for monotonic loading
$\epsilon_{s,m}$	bar average strain	τ_{a0} loading bond stress in the first loading cycle
$\epsilon_{s,FOM}$	FOM strains	$\tau_{a\infty}$ loading bond stress after large number of unloading-reloading cycles
$\epsilon_{s,t}$	top bar strain obtained with FOM measurements	τ_i loading bond stress after unloading
$\epsilon_{s,b}$	bottom bar strain obtained with FOM measurements	τ_{i0} loading bond stress after first unloading
E_s	elastic steel modulus	$\tau_{i\infty}$ unloading bond stress after large number of unloading-reloading cycles
f_c	concrete cylinder compressive strength	τ_{max} peak bond stress calculated from FOM strains
f_y	yield strength of reinforcement	τ_{west} bond stress of the fibre close to the free surface
$f_{ct,eff}$	concrete effective tensile strength	τ_{east} bond stress of the fibre at the inner side
ϕ	bar diameter	u horizontal crack opening
l_{ba}	transfer length	u_A horizontal crack opening in section A
$l_{ba,max}$	maximum transfer length	v beam deflection
l_{bi}	unloaded transfer length	v_{max} maximum beam deflection
M	bending moment	V applied shear force
n_{cycles}	number of cycles	$V_{cycl,max}$ maximum level of shear force applied on beams
N	normal force	$V_{cycl,min}$ minimum level of shear force applied on beams
ψ	rotation of the shear crack	V_R ultimate shear resistance
ρ	reinforcement ratio A_s/A	V_s dowelling force of reinforcement
R	target ratio between maximum and minimum applied forces	w_c maximum crack width at which concrete tensile softening stresses are transmitted
σ	average stress of the tie	crack width after unloading
σ_s	average stress in the reinforcement	w_{per} crack width after unloading
$\sigma_{s,FOM}$	stress in the reinforcement calculated with FOM strains	x position along the specimen
$\sigma_{s,cracked}$	stress in the reinforcement calculated according to an	z lever arm

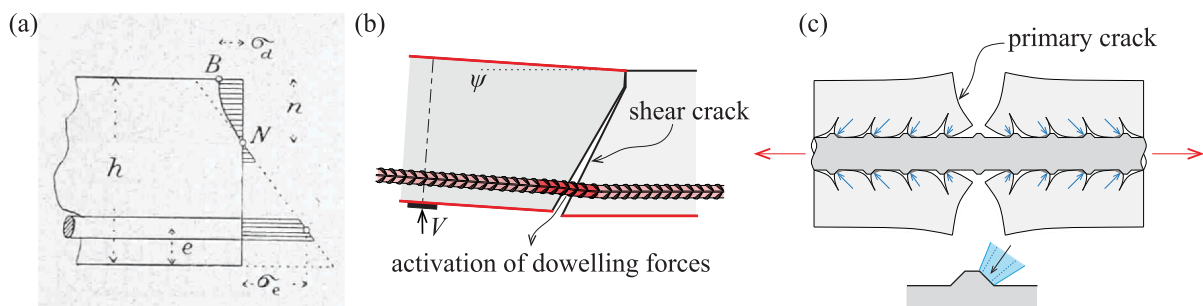


Fig. 1. Rebar-to-concrete interactions: (a) bending of the reinforcement according to Ritter [1]; (b) dowel action; and (c) mechanical rib engagement with cracks according to Goto et al. [4].

glued on the bar surface or providing a measurement near the bar axis if glued on longitudinally-cut bars). These techniques have however been significantly improved in recent times. With respect to data acquisition on concrete surface (strains and displacement fields), a notable step forward has been performed with Digital Image Correlation (DIC) measurement systems [9]. DIC enables detailed and continuous readings of the displacement field on the concrete surface [10] allowing to calculate on that basis strain fields and relative displacements of crack lips. This has allowed for detailed understanding of the kinematics developed by shear and flexural cracks [11] and their associated

understanding of load-carrying actions [12,13].

Although concrete surface data gathered by DIC can be used for evaluation of the reinforcement response (as dowel action, [13]), this technique provides no direct measurements on the local strain state of the reinforcement bars. With this respect, the implementation of Fibre-Optical Measurement systems (FOM, [14]) in steel rebars is allowing for high quality readings on the surface of reinforcement. FOM allows for continuous readings along a bar at different locations and at high frequencies. This allows observing high strain gradients in a bar, along its axis and for different locations of the cross section.

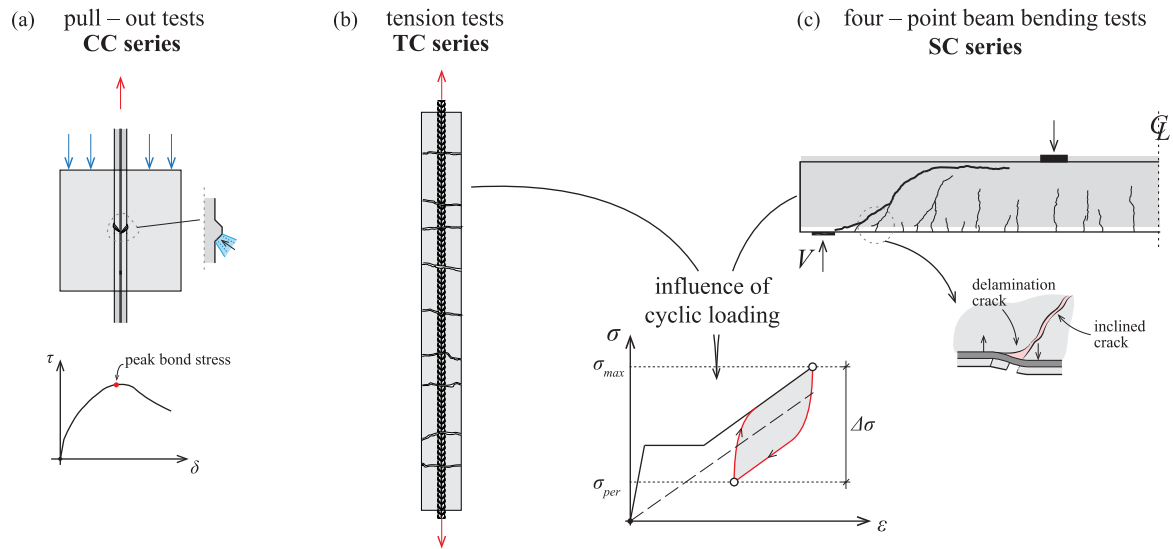


Fig. 2. Experimental investigation on: (a) monotonic pull-out tests; (b) tensile tests subjected to cyclic loading; (c) four-point bending tests on beams subjected to cyclic loading.

Recent works [15–21], have shown that the acquisition of strain measurements on reinforcement surface could provide detailed information about the interactions engaged between reinforcement and the surrounding concrete with respect to the cracking stage and the cyclic degradation of concrete. Amongst the first experiences, it is relevant to cite the works by Davis et al. [17] focusing on bare bars and reinforced concrete ties investigated by means of fibre optic strain measurements. Also, detailed developments on distributed sensing techniques for the loading response of large reinforced concrete members have been performed by Poldon et al. [19] and Brault et al. [20] in conjunction with surface measurements. More recently, FOM sensors used for detection of degradation mechanisms related to cyclic loading have also been implemented by Broth et al. [21].

By making use of these techniques, this paper revisits the results of classical tests on reinforced concrete elements by means of detailed measurements performed with FOM glued on the surface of steel rebars combined with DIC readings for concrete surface. The investigation focuses on three different types of structural elements addressing a

number of responses:

1. Two pull-out tests – Evaluation of stress concentration at the ribs of rebars, Fig. 2a.
2. Eight tension tests for bare and embedded reinforcement subjected to cyclic loading: detailed analysis of residual crack openings and negative tension-stiffening, Fig. 2b.
3. Three four-point bending tests on beams failing in shear subjected to cyclic loading: development of curvatures at the reinforcement, dowel action and development of cover delamination due to kinematic compatibility, Fig. 2c.

The results show the complexity of the interactions between reinforcement and the surrounding concrete as well as the influence of compatibility of deformations on their response. On this basis, a number of implications for practical design are presented and discussed.

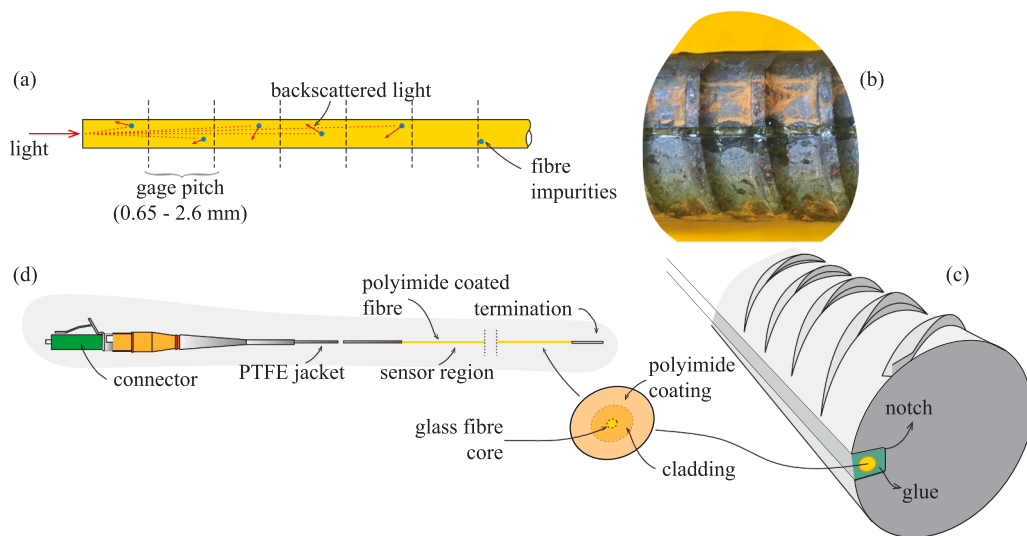


Fig. 3. FOM measurements: (a) back-scattering mechanism due to fibre core impurities; (b) view of the fibre-optic sensor glued to a steel rebar; (c) sketch of the fibre optical cable placed in the groove and adhering to the steel due to two-component glue and (d) description of the fibre optical cable structure with angle polished connector on one side and termination which avoids light reflection.

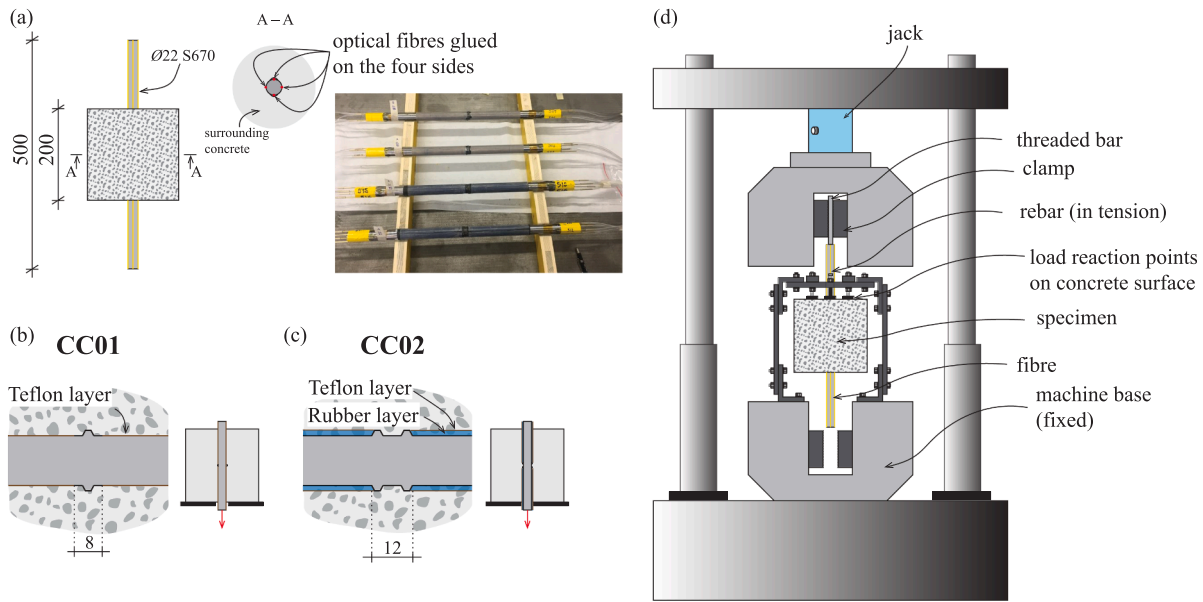


Fig. 4. Pull-out tests: (a) sketch of the specimens with focus on the optical fibres glued on the rebar surface; (b) pull-out test type CC01 for the investigation of concrete crushing (one rib); (c) pull-out test type CC02 for the investigation of shearing-off between ribs; and (d) view of the test setup (units in mm).

2. Experimental programme

All experiments have been carried out in the Structural Concrete Laboratory of École Polytechnique Fédérale de Lausanne (Switzerland).

Measurement techniques

For DIC measurements, pictures were generally acquired with a frequency ranging between 0.5 and 2 Hz, using two SVCam-hr29050 sensor cameras (29 Mpx), in combination with controlled lighting conditions. Random speckle pattern was applied on the concrete surface by means of spray painting (with a size of 1 ± 0.5 mm). The displacement analysis was then performed with Vic3D software [9], using a subset size of 29×29 pixels yielding to a displacement error below 1/50 times the size of the pixel (pixel size: 500 μ m).

Moreover, strain measurements on the rebar surface based on Rayleigh scattering [22] were used (Odisi-B version by Luna Innovations [14]). Odisi-B version performs measurements by means of an Optical Frequency Domain Reflectometry (OFDR) which allows obtaining strain profiles at relatively high sampling rates and refined spatial resolution (with an error in the strain measurement of about 25 μ ϵ). Regarding fibre optics, its structure may be split in three main components (see Fig. 3): core, cladding and coating. The core is the medium in which light is propagating, the cladding allows transmitting the light exclusively along the fibre optical sensor. The coating is an external protection which prevents the core to be damaged. In this research, polyimide coating was used ensuring negligible slip between the core and the medium in which the fibre optical cables were embedded. Fibre optics were embedded along steel rebars according to the procedure as follows:

- I. 1 mm-depth grooves were performed along two or four sides of the rebar by means of a thin cutting disc on an angle grinder which was fixed to a cart in order to maintain the alignment of the notch with respect to the rebar (the area of each groove was about 3 mm² corresponding to a bar area reduction per groove of about 3.80% in ϕ 10 bars, 0.95% in ϕ 20 bars and 0.79% in ϕ 22 bars).
- II. 125 μ m polyimide fibre optics were placed at the bottom of the groove and fixed with scotch tape to ensure the position of the fibre. Two-component glue was then placed in the groove avoiding relative slip between the fibre and the steel rebar.

- III. An Angle-Polished Connector was then spliced at one end of the fibre glued in the groove. The connector was necessary to send a light wave into the core through Odisi-B interferometer. On the other end of the fibre, a termination was then provided avoiding reflection of the light.

During the measurements, 0.65 mm spatial resolution was used (*i.e.* gage pitch). Depending on the test, two or four fibres were installed on the bars (the gage pitch provides the maximum possible spatial resolution of the system).

3. Pull-out tests

3.1. Main parameters and test setup

Two pull-out tests were performed with the aim of investigating the interaction between concrete and ribs on the rebar surface, see Fig. 4a. Two types of tests were carried out to investigate two different failure modes (local crushing or shearing-off) occurring at the rebar-to-concrete interface.

For test CC01, all ribs but one were mechanically removed from the bar: the contact between the rebar and the concrete was in addition disabled by placing a thin layer of Teflon (see Fig. 4b). This test aims at investigating the contact forces between one rib and the surrounding concrete in case of local crushing, Fig. 4b. In test CC02, all ribs but two were removed and bond was disabled except between the investigated ribs by arranging a rubber layer sufficiently thick (2 mm) to avoid engaging of the first rib. To avoid friction between concrete and rubber, a thin Teflon layer was placed on top of it. This test was addressed at the resistance of concrete between ribs to be sheared - off (see Fig. 4c).

The rebars were equipped with four optical fibres glued in 1-mm depth grooves and embedded in 200 \times 200 mm concrete cubes (Fig. 4). All specimens were cast with normal-strength concrete whose compressive strength at the day of testing ranged between 41.0 and 42.6 MPa (average of three compressive tests on 160 \times 320 mm concrete cylinders). The maximum aggregate size was 16 mm for all test specimens. The cement was CEM II/B-M (T-LL) 42.5 N, in accordance with [23], with a water-to-cement ratio equal to 0.53. The embedded rebars ϕ 22 consisted of high-strength (S670) steel with a yield strength $f_y = 701$ MPa determined according to EN ISO 6892-1 (0.2% of residual

Table 1
Main parameters of pull-out tests.

Specimen	f_c , [MPa]	ϕ , [mm]	rib spacing, [mm]	f_y , [MPa]	Type
CC01	41.0		8.2		one rib (Teflon)
CC02	42.6	22	8.2	701	two ribs (Teflon + rubber)

plastic strain, refer to the details in Table 1). Ribs were approximately 1 mm–height and 8.2 mm–spaced leading to a measured bond index f_R of 0.12 (evaluated by surface scan). During casting, the bar was placed horizontally.

The test setup is presented in Fig. 4d. All tests were performed according to a displacement–control protocol with a displacement rate ranging between 0.01 mm/s (ascending branch) up to 0.05 mm/s (softening branch). The typical duration of one test was about 2–8 min up to reaching the maximum load.

3.2. Test results

The measured bond–slip curves are presented in Figs. 5a–b. The relative slip between the rebar and concrete surface was measured by setting a Linear Variable Differential Transformer (LVDT) on the loaded bar end while the bond stress is averaged on the area defined by the nominal perimeter ($\pi \cdot 22$ mm) times the rib spacing (8.2 mm). The measured strains on the sides of the rib (blue and red lines for compression and tension values, respectively) is additionally shown as a function of the bond stresses τ in Figs. 5c–d.

As it can be seen in Fig. 5, the overall behaviour for different failure modes investigated differs considerably in terms of maximum peak stresses as well as the potential displacement capacity in the softening branch. For test CC01, the peak is reached for an average bond stress τ of

59.2 MPa, corresponding to a relative slip at peak load of 6.45 mm. After reaching the maximum load, the response was relatively tough (only small decrease of the bond stress with increasing slips up to 10 mm) during the softening phase, see Fig. 5a.

With respect to the shear – off failure corresponding to test CC02 (Fig. 5b), failure occurred at lower average bond stresses τ , of about 20 MPa. The associated slip was also lower, around 1.1 mm and the test followed later a relatively brittle response in the softening phase (60% strength reduction develops for slips ranging between 2.5 and 5.5 mm which can be explained by the reduction of the contact area with increasing slip as shown with the dotted line in Fig. 5b).

The longitudinal strain profiles measured from the analyser are shown in Fig. 5e and Fig. 5f for tests CC01 and CC02 respectively (with positive strains referring to member elongation). Several loading steps are selected between 5% and 100% of the maximum measured bond stress τ . Fig. 5e and Fig. 5f show a strong gradient of strains at the vicinity of the rib due to engagement of contact forces between concrete and ribs. Several phenomena can be observed with respect to the response of the specimens. For test CC01, the surface strains can reach in the vicinity of the rib very high values (even higher than the yield strain of about 3.5 mε) despite the low average bar strain values (≈ 0.5 mε, calculated by dividing the maximum force by the nominal cross section of the bar and the elastic modulus).

Such concentrations of strains localize in a region with a length similar to one diameter before and after the rib (total disturbed zone of approximately two bar diameters). The length of the disturbed zone is however not constant. It increases for low values of τ up to approximately 25 MPa. Thereafter (refer to values above 40 MPa in Fig. 5e), the length of the disturbed zone remains roughly constant.

During the first phase, the strains in both sides of the ribs increase roughly linearly (Fig. 5c). Thereafter, once the disturbed zone does not increase in length, the strain increases more than proportionally (refer to sudden change of slope in Fig. 5c). This can also be observed in the bond – slip curve (Fig. 5a) associated to a softer response. Moreover, as can be

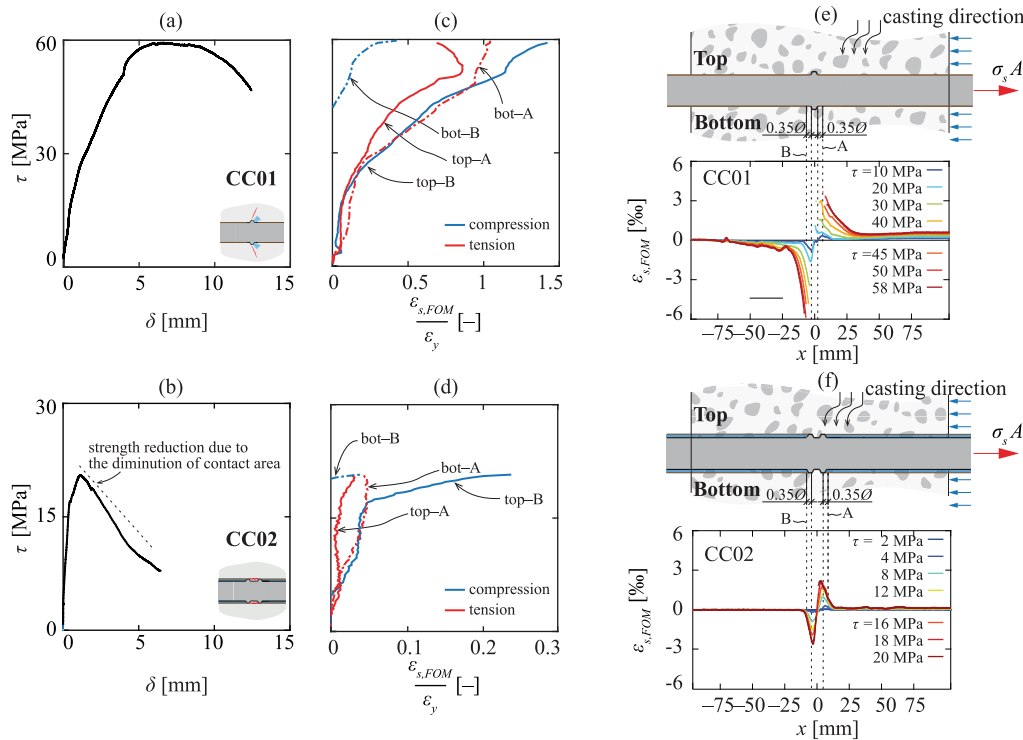


Fig. 5. Pull-out tests results: bond stress τ – slip δ in the rebar for specimens (a) CC01 and (b) CC02; bond stress τ – normalized strain $\epsilon_{s,FOM}/\epsilon_y$ for top (continuous lines) and bottom (dashed lines) fibres in sections A and B for specimens (c) CC01 and (d) CC02 (sections A and B are located at 0.35ϕ from rib edges); profiles of measured strains $\epsilon_{s,FOM}$ in top fibre (with respect to casting direction) for specimens (e) CC01; and (f) CC02.

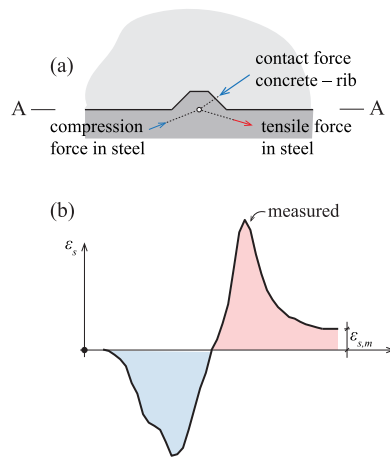


Fig. 6. Mechanical engagement of bond: (a) forces at concrete–rib interface; and (b) measured strain profile at section A–A.

seen in Figs. 5c–d, even if these cases should represent “good bond conditions” according to Eurocode 2 [24], rather different level of strains are recorded at the top and bottom side of the bar with respect to the casting direction. This difference can potentially be explained by the voids under the bar resulting from bleeding and plastic settlement of fresh concrete just after casting [25].

A similar response is also observed for test CC02 (two ribs) with the same development of two regimes (Fig. 5f). The length of the disturbed zone is in this case smaller and comparable to the rib distance (0.4 times the bar diameter). The failure at a lower load and more brittle response can in this case be associated to the shear – off of concrete between ribs (Fig. 5b) limiting the contact area with increasing slip.

3.3. Interpretation of test results

The experimental results have shown a number of phenomena governing the rebar-to-concrete response:

- Strong strain (and stress) gradients occur near the ribs.
- Such disturbances are located at the surface in regions not larger than one bar diameter. When more than one rib is engaged, the disturbed zone with strain concentrations and gradients at the surface may develop in the whole distance between ribs.
- The surface strains can locally attain very high values. In the performed tests, although the average bar strain was well beyond the yield threshold of the bar (about 25% of the yield strain), the surface strains indicated locally values above the yield strain.

A potential explanation of the observed response may be found in the spreading of the local contact forces in the rebar, developed at the rib as shown in Fig. 6a. The measured strain profile over the line A–A (Fig. 6b) is consistent with the development of compressive and tensile stresses in

the bar which carry the contact force between the concrete and the rib. Such stress concentrations can thus be detrimental to the fatigue strength of the reinforcement bar. This is in agreement with the observation that the fatigue strength of bars embedded in concrete is typically lower than the fatigue strength of bare bars [26]. It shall however be noted that when the strength in a concrete member is governed by the reinforcement, the rebar sections at the cracks reach yielding. This implies that, at the crack location, no rib-to-concrete interaction happens, and in the vicinity, the plastic lateral contraction of a bar reduces (together with resistance of local punching cracks [4]) the bond stresses.

4. Tension tests

4.1. Main parameters and test setup

Five tension tests subjected to cyclic loading were performed on prismatic reinforced concrete ties with 100×100 mm square cross section and 1150 mm side length (consistently with the experimental programme of Farra and Jaccoud [27]). They were completed with three additional tests on bare rebars. The specimens were reinforced with one single rebar placed either centred with respect to the cross section of the tie (TC04, TC05, TC06) or eccentric (TC07, TC08). All members were tested under cyclic loading with a nominal target ratio R between the minimum (σ_{min}) and the maximum (σ_{max}) stress in the rebar equal to 0.10 ($\sigma_{max} = 275$ MPa and $\sigma_{min} = 27.5$ MPa). The maximum applied stress (σ_{max}) was set at 275 MPa and was kept constant for all tests. The tests were displacement-controlled with a displacement rate ranging between $0.5 \mu\text{m/s}$ (embedded rebars) and 0.05 mm/s (bare rebars). In the reinforced ties, this led to approximately two minutes to perform one cycle, except for the first cycle in which a reduced strain rate ($0.1 \mu\text{m/s}$) was imposed in order to properly follow the cracking process. For every test, the loading protocol consisted of 100 cycles according to the displacement rate mentioned above. All specimens were cast with normal-strength concrete whose compressive strength at the day of testing ranged between 35.3 and 35.7 MPa. Direct tension tests on concrete cylinders were also performed showing a tensile strength at 28 days of 2.1 MPa. The maximum aggregate size was 16 mm for all test specimens. The cement used was CEM II/B-M (T-LL) 42.5 N, in accordance with [23], with a water-to-cement ratio of about 0.5.

The longitudinal reinforcement consisted of $\text{Ø}10$ cold – worked rebars (yield strength calculated according to EN ISO 6892-1 [28]), $\text{Ø}20$ hot-rolled reinforcing bars with a well-defined yield plateau and high-strength S670 $\text{Ø}22$ reinforcing bars (yield strength calculated according to EN ISO 6892-1 [28]). Three nominal reinforcement ratios were investigated ranging between 0.78 % and 3.80 %. Refer to details in Table 2 and Fig. 7a. The specimens were cast horizontally in the position shown in Fig. 7b.

Fig. 7c shows the test setup adopted in the current programme. Tests were performed by clamping the bottom side of the rebar and pulling upwards on the top side of the specimen (using a Schenck hydraulic jack with a total capacity of 1 MN). Rebars were equipped with four optical fibres glued on the four sides while concrete surface behaviour was

Table 2
Main parameters of tensile tests*.

specimen	Ø , [mm]	ρ , [%]	type	position	f_c , [MPa]	f_y , [MPa]	COV, [%]
TC01	10		bare	–	–	539	0.42
TC02	20					518	0.11
TC03	22					701	0.43
TC04	10	0.78	embedded	centred	35.3	539	0.42
TC05	20	3.14			35.5	518	0.11
TC06	22	3.80			35.5	701	0.43
TC07	20	3.14		ribs against sides	35.6	518	0.11
TC08	20	3.14		ribs against cover	35.7	518	0.11

* COV refers to the yield strength of reinforcement.

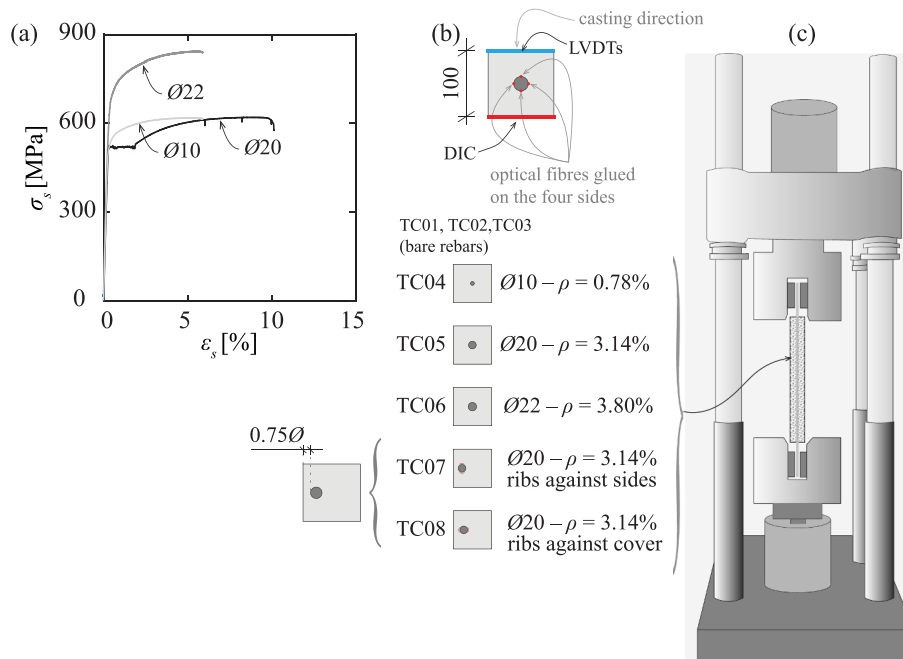


Fig. 7. Tensile tests: (a) measured stress–strain relationships of reinforcement bars; (b) specimen cross section and main mechanical properties; (c) front view of test setup.

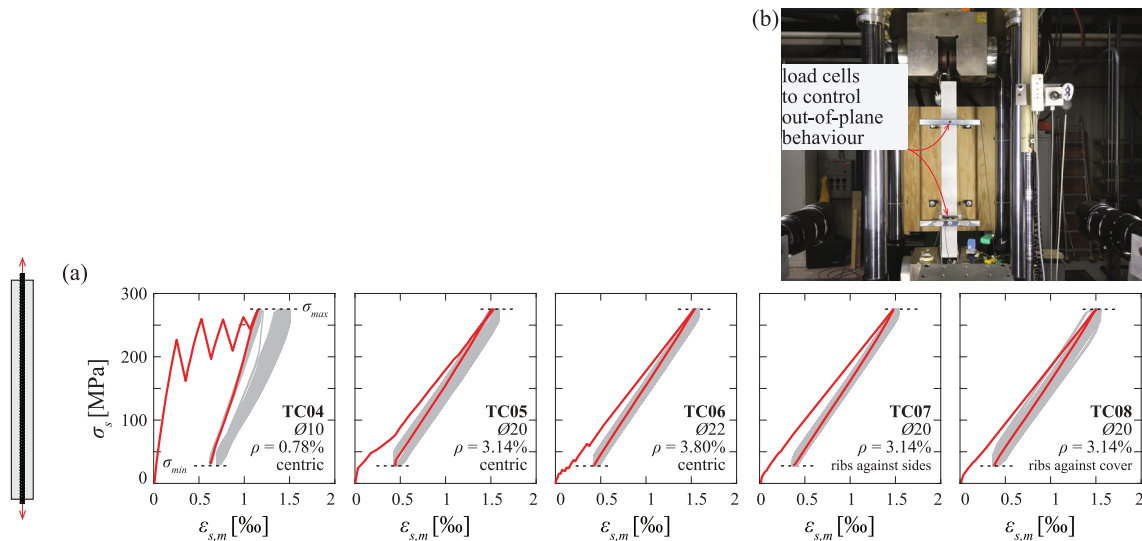


Fig. 8. Tensile tests: (a) steel average stress – local average strains for embedded rebars under cyclic loading; and (b) front view of test setup for eccentric rebars (refer to red curves for first loading cycle and grey curves for envelope of all cycles). (For interpretation of the references to color in this figure legend, the reader is referred to the web version of this article.)

tracked by performing DIC and LVDTs measurements on two opposite sides of the specimens (see Fig. 7).

Out-of-plane displacements of the eccentrically loaded specimens needed to be controlled in order to avoid splitting of the concrete cover close to the edges of the member (due to clamping effect of the loading machine). Thus, two symmetric load cells were placed along the member in order to control out-of-plane behaviour.

4.2. Test results

The measured average steel stress (total force divided by cross section area of steel bar) – average steel strain curves are presented in Fig. 8 both for reinforced concrete tension members with centred rebars (TC04, TC05, TC06) and for members with eccentric rebars (TC07,

TC08). The average steel stress is calculated as the applied tensile force divided by the nominal rebar area (calculated as $\pi\phi^2/4$). As for the previous tests, four fibres were glued in the rebars. In Fig. 8, the average local steel strain is calculated by averaging the local longitudinal steel strains resulting from FOM measurements over the whole length of the concrete tie.

The observed cracking patterns of the tested specimens loaded until failure are illustrated in Fig. 9. Cracks developed mostly perpendicular to the longitudinal direction of the member and its spacing was largely governed by the reinforcement ratio. During first loading, primary cracks formed and cracking was stable during the cycles except for specimen TC04 in which the last primary crack developed during the second load cycle (refer to stress–strain curve in Fig. 8a and to Fig. 9). After the load cycles and during final loading to failure, additional

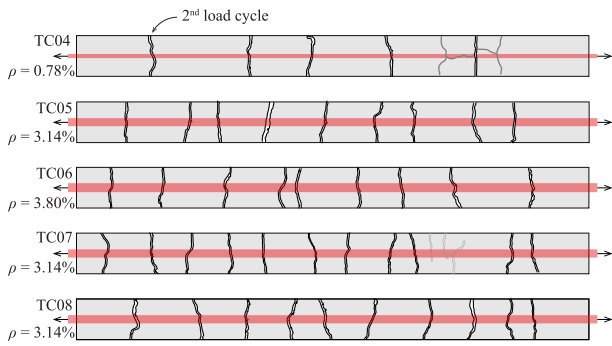


Fig. 9. Tensile tests: cracking patterns of tested specimens (cracks in light grey developed after all load cycles, during monotonic loading up to failure; for specimens with eccentric bars, the surface on the bar's side is shown).

secondary cracks developed as well as splitting cracks parallel to the reinforcement (refer to cracks in light grey in Fig. 9).

Fig. 10 presents the strain results developed during the loading process including 100 cycles of loading and unloading, ranging between

the maximum rebar stress $\sigma_{max} = 275$ MPa and the minimum stress $\sigma_{min} = 27.5$ MPa. The steel stresses were calculated from the measured longitudinal strains (with a spatial resolution of 0.65 mm) by smoothing over a length equal to two times the bar diameter (in agreement to the disturbed length observed in the pull-out tests) and by assuming $E_s = 200000$ MPa. Details of the response for an unloading cycle (after six loading cycles) are also presented in Figs. 10b-d.

Several outcomes may be highlighted from these results. A first fact refers to the profiles of stresses (Fig. 10c derived from the FOM measurements). Before unloading (load level LL1 in Fig. 10c), it can be noted that the maximum stress develops at the location of the cracks with a rather linear decrease of stresses at the sides. This observation is relatively in fair agreement with the consideration of a constant bond law between the bar and the concrete (as adopted for instance by the tension chord model [29,30]).

This result is confirmed by the calculated bond stresses τ_b derived from equilibrium considerations:

$$\Delta\sigma_s \frac{\pi}{4} \phi^2 = \tau_b \pi \phi \Delta x \rightarrow \tau_b = \frac{\phi}{4} \frac{\Delta\sigma_s}{\Delta x} \quad (1)$$

As presented in Fig. 10d, the calculated values show a plateau

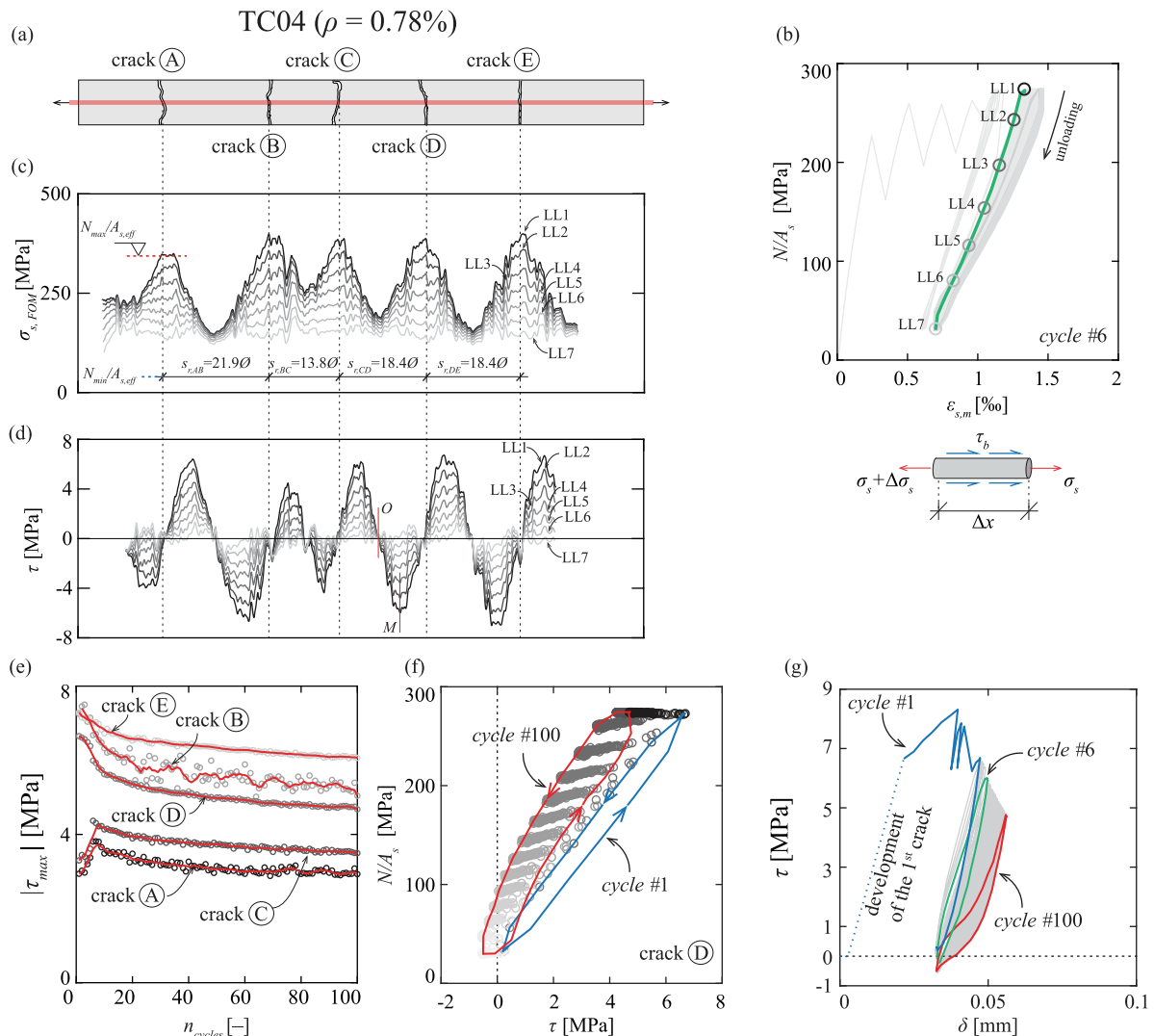


Fig. 10. Tensile tests – specimen TC04: (a) cracking pattern in the cyclic loading phase; (b) stress-strain relationship for all cycles (in grey) and cycle #6 (in green) indicating load levels; (c) profiles of stresses $\sigma_{s,FOM}$ calculated on the basis of measured strains (FOM) and (d) profiles of bond stresses τ along the steel rebar; (e) bond stresses degradation for the selected cracks due to cyclic loading as a function of number of cycles (peak bond stress τ_{max}); (f) bond stresses in the loading and unloading phases as a function of the stress N/A_s in the rebar during cyclic loading; and (g) bond-slip relationship for a section located at maximum bond stress (3ϕ from the crack). (For interpretation of the references to color in this figure legend, the reader is referred to the web version of this article.)

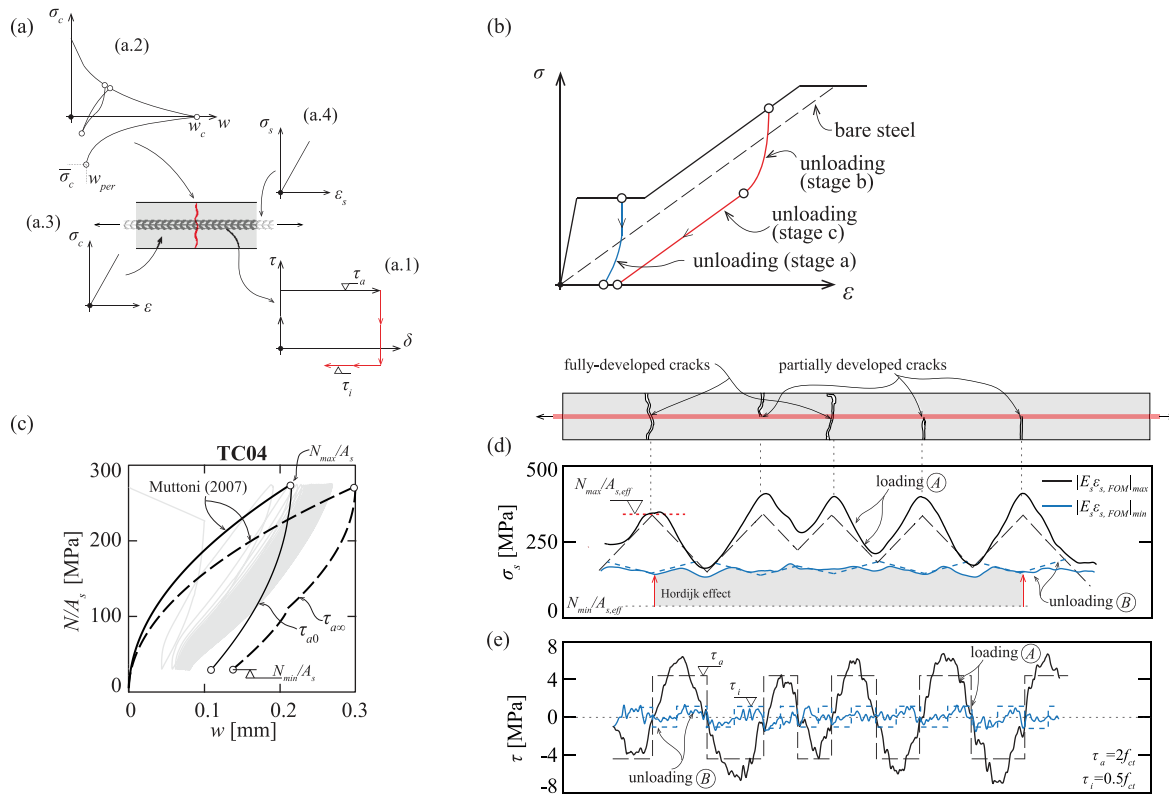


Fig. 11. Negative tension-stiffening: (a) assumptions of approach by Muttoni and Fernández Ruiz [32]: (a.1) bond between concrete and reinforcement under cyclic loading (rigid-plastic law); (a.2) concrete response (Hordijk [37]); (a.3) elastic behaviour of concrete; (a.4) elastic behaviour of steel; (b) stress-strain response of reinforced concrete tie and different unloading stages; comparison of analytical model by [32] ($k = 0.95$, $\tau_a = 2f_{ct,eff}$, $\tau_i = 0.5f_{ct,eff}$) with test results obtained for tie TC04 ($\rho = 0.78\%$) with respect to (c) loading average stress (N/A_s) – average crack opening (w); (d) steel stress distribution and (e) bond stresses distribution for steel stress corresponding to $N_{max}/A_{s,eff}$ (black lines) and $N_{min}/A_{s,eff}$ (blue lines). (For interpretation of the references to color in this figure legend, the reader is referred to the web version of this article.)

ranging between 5 and 7 MPa, in good agreement to the expression for this purpose proposed by Martí et al. [29]:

$$\tau_b = 0.6f_c^{2/3} \quad (2)$$

During unloading (refer for instance to load level LL7 of cycle #6 in Figs. 10c–d), the bond stresses reduce and reach even negative values (as consistently adopted in approaches reproducing negative tension-stiffening [31–34]). This yields eventually to a relatively constant value of the stresses along the bar. It is interesting to note that, except at the location of cracks, the steel bar is subjected to a stress range which is fairly lower than the one corresponding to a bare bar (this yields to implications on the fatigue response of ties as it will be later discussed).

Another interesting fact that can be directly derived from FOM is the degradation of bond with increasing number of cycles, Fig. 10e. This phenomenon has been already observed by a number of researchers [35–38,8,7,5]. A clear degradation can be observed particularly at the first loading cycles but without stabilization after 100 cycles. This trend seems to confirm the reductions proposed by Tassios [35] and Balázs [8], with a reduction of 30% of the uniform bond strength after cyclic loading. Also, the same phenomenon is observed for the bond values in the unloading phase (Giuriani [39]), as can be seen in Fig. 10f, in which bond degradation could be outlined as a function of the level of steel stress.

A more detailed insight of the bond degradation with cycles is presented in Fig. 10g as a bond-slip relationship for the section with maximum bond stresses (section M in Fig. 10d). The slip is calculated by integration of average rebar strains (assuming negligible concrete strains) from the point with no relative slip (section O in Fig. 10d). During the first monotonic loading (blue part), the results show both the bond activation and the small unloading steps happening when new

cracks develop under controlled deformation (sudden drops in the force and in the bond stress). During the first total unloading, the bond stresses were not negative, but close to zero. As the number of cycles increased, the maximum bond stress reduced following the degradation of bond, and negative values of the bond stress were also reported (in close agreement to the observations of Giuriani [39]). One can also observe that the bond degradation during the small unloading steps due to the development of new cracks is of the same order of magnitude of the degradation during the 100 loading and unloading cycles. Consistent measurements were also obtained for other sections of the rebar.

4.3. Interpretation of test results

As already outlined in Section 1, structural concrete is a composite material in which the understanding of the mechanical engagement between the concrete matrix and steel interface (bond) is instrumental for the evaluation of crack widths and the overall stiffness of cracked concrete members (both under service conditions or at failure [32–34]). So far, several mechanical models accounting for tension-stiffening by means of simplified or realistic bond-slip laws have been proposed mostly addressed to the case of monotonic loading [29,30,40]. Fewer approaches exist on the response of concrete members subjected to cyclic or fatigue loading, in particular with respect to the evaluation of residual crack openings and the negative tension-stiffening effects [32,34].

The physical approach proposed by [32] will be adopted in the following for the interpretation of the test results of the experimental programme performed on tension members and beams. The main assumptions of this approach [32] are highlighted below (details of the equations of [32] used for the comparisons presented in this paper are

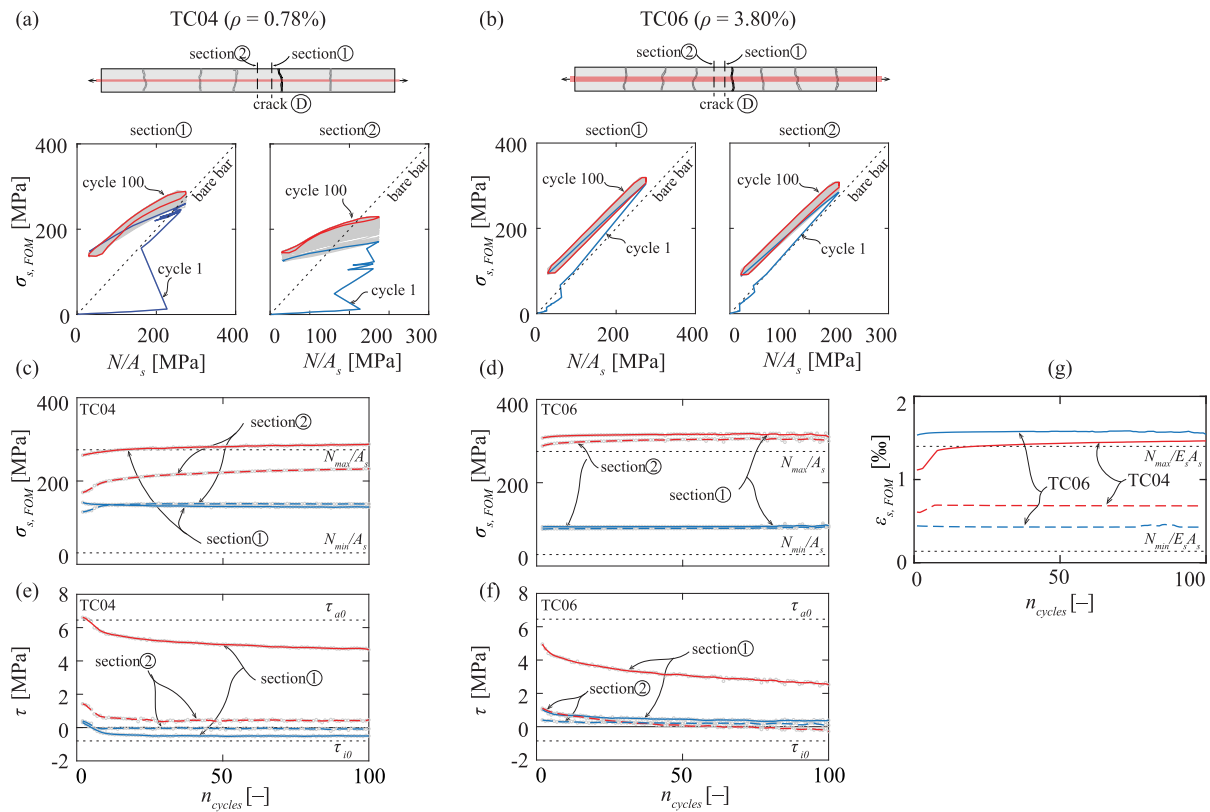


Fig. 12. Average stress in the loading/unloading phase N/A_s with respect to calculated stresses $\sigma_{s,FOM}$ on the basis of measured FOM strains for specimens (a) TC04 and (b) TC06 (refer to blue curves for first load cycle and red curves for last cycle); calculated stresses $\sigma_{s,FOM}$ on the basis of measured FOM strains at the maximum loading stress N_{max}/A_s (red curves) and minimum loading stress N_{min}/A_s (blue curves) with the number of cycles for specimens (c) TC04 and (d) TC06; bond stresses τ at the maximum loading stress N_{max}/A_s (red curves) and minimum loading stress N_{min}/A_s (blue curves) for specimens (e) TC04 and (f) TC06 (values plotted in section 1 at the location of peak bond stress and section 2 located in-between cracks); and (g) average strains in the tie at the maximum loading stress N_{max}/A_s (continuous lines) and minimum loading stress N_{min}/A_s (dotted lines) with the number of cycles. (For interpretation of the references to color in this figure legend, the reader is referred to the web version of this article.)

given in Appendix A):

- Bond between concrete and reinforcement is assumed to follow a rigid-plastic law (Fig. 11a.1). As already shown in Fig. 10c, this approach leads to reasonable results (relatively constant values of bond stresses between cracks).
- The concrete response at the cracks (including softening, unloading and residual opening due to imperfect closure of cracks) is accounted for by means of the approach proposed by Hordijk [37], considering also residual crack openings due to imperfect crack closure (Fig. 11a.2). In-between cracks, concrete is assumed to have an elastic response (whose strains are generally neglected), Fig. 11a.3.
- Reinforcement is assumed to remain elastic, Fig. 11a.4.

On this basis [32], the loading and unloading response can be characterized by three regimes of behaviour, see Fig. 11b:

- **Stage a:** unloading during the crack development phase.
- **Stage b:** unloading during the stabilized cracking phase where bond stresses may correspond to loading or unloading conditions.
- **Stage c:** unloading during stabilized cracking phase where bond stresses correspond only to unloading conditions.

The results of this approach are compared in Figs. 11c–e to the experimental measurements for the representative specimen TC04. As presented in Fig. 11c, despite the strong simplification of the behaviour, the analytical model reproduces in a suitable manner the relationship between the average crack opening and the steel stress, in particular, if

bond degradation after a number of cycles is accounted for (refer to the dashed line in Fig. 11c). The analytical results in terms of steel stresses and bond stresses, Figs. 11d–e, were obtained by setting the location of the cracks at the actual ones and calculating the slopes of the stress profile on the basis of the governing bond strength:

- $\tau_{a0} = 0.6f_c^{2/3} \epsilon$ for loading under short-term conditions [29,32].
- $\tau_{a\infty} = 0.7\tau_{a0}$ for cyclic loading conditions [8,35].
- $\tau_{i0} = 0.15f_c^{2/3}$ for unloading under short-term conditions [29,32].
- $\tau_{i\infty} = 0.5\tau_{i0}$ for cyclic unloading conditions [39].

In addition, it shall be observed that, in specimen TC04, all cracks did not fully develop along the whole cross section during cyclic loading (refer to cracking pattern in Fig. 11). In these cases, the bars experienced local bending, which justifies why the measured steel stresses are in certain cases above the threshold of $N_{max}/A_{s,eff}$ (where $A_{s,eff}$ is the effective area of the bar accounting for the reduction due to presence of four grooves).

On the whole, the comparison shows a satisfactory agreement (particularly in fully-developed cracks) and a realistic reproduction of the different phenomena (bond slopes, short-term and cyclic loading conditions) are suitably reproduced. This analysis shows that, at the location of the cracks, the stresses vary according to the external applied force and the residual stresses generated by the imperfect closure of cracks (refer to Hordijk’s effect in Figs. 11a.2,d). In-between cracks, however, the difference of stresses is significantly lower due to the bond stresses. This might be a potentially favourable effect with respect to fatigue issues (refer to the grey-shaded region in Fig. 11d in which the

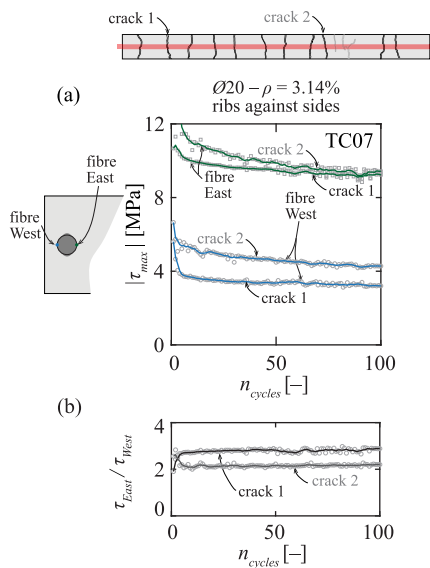


Fig. 13. Specimen TC07 with eccentric bar: (a) bond stress degradation; and (b) ratio between maximum bond stresses of fibre at the inner side (fibre East) and fibre close to free surface (fibre West) for two selected cracks.

imperfect crack closure of crack lips leads to larger stresses in the bar). The global response of the tie seems to be mostly influenced by the total amount of available reinforcement. This leads to different development of the maximum–minimum steel stresses with the number of cycles as well as in terms of maximum and minimum average strains of the tie. Fig. 12 presents for instance, a comparison of the behaviour at the location of a selected crack (refer to crack D in Figs. 12a–b) for specimens TC04 and TC06 (with reinforcement ratios equal to 0.78% and 3.80% respectively). The steel stress behaviour is presented in two critical sections, Fig. 10d:

- Section 1 corresponding to the location of the peak of bond stress τ_{max} at the vicinity of crack D (refer to Figs. 12a–b).
- Section 2 located in-between two cracks, as shown in Fig. 12.

As can be seen from the hysteretic behaviour in Figs. 12a–b in terms of resultant steel stress N/A_s and measured steel stress $\sigma_{s,FOM}$, the effects of residual concrete tensile strength at maximum load and compressive stresses in concrete at minimum load can be clearly outlined from the evolution of steel stresses between the first and the last cycle.

In particular, the evolution of the residual concrete tensile strength may be identified in the loading branch of the first loading cycle in which after the unstabilized cracking process, the steel stress at the crack approaches that of a bare bar. Then, negative tension-stiffening effects and the compressive stresses in concrete at the crack section develop

with the number of cycles. This gives rise to steel stresses at the crack which are larger than the stresses of a bare bar, especially at the minimum level of stress σ_{min} . This fact can represent a favourable effect with respect to fatigue verification, since reduced stress variations develop on the reinforcement at the crack section. This aspect seems to be more pronounced in specimen TC04 with a low reinforcement ratio (and thus higher influence of bond stresses in the response) leading to minimum stresses in the reinforcement larger than the ones for specimen TC06 (with higher reinforcement ratio). With respect to concentrations of stresses, the section in-between cracks (Section 2 in Figs. 12a–b) is the least critical, associated to the lowest variation of stresses. The largest variation of average stress occurs at the location of the crack (with only differences with respect to a bare response due to the effect of imperfect closure of cracks as described by Hordijk, Fig. 11a.2). However, in terms of local stress variations near the surface of the bar, probably the most critical section is at the location with the most unfavourable combination of variation of average stresses and stress gradients related to bond and stress concentrations near ribs.

Regarding steel strains at minimum load (dashed lines in Fig. 12g) and maximum load (continuous lines in Fig. 12g), the following issues may be outlined:

- The reinforcement ratio plays a significant role with respect to the residual strain of the tie: larger residual strains can be observed after several cycles for lower reinforcement ratios, attaining maximum values which range between 1 and 3.5 times the values of bare bars.
- The average strain at N_{max}/A_s increases with the number of cycles leading to larger crack openings.
- These aspects could be detrimental for service limit state verifications (higher crack widths with increasing number of cycles), but potentially beneficial for fatigue in case of redistribution of internal forces.

With respect to the behaviour of eccentric bars, its response is shown in Fig. 13a–b for specimen TC07 (with ribs against the sides). Differently from tests with centred bars in which bond stresses are relatively uniform around the perimeter of the bar, when the bar is eccentric, the distribution of bond stresses is no longer uniformly distributed along the control perimeter of the bar. Fig. 13a presents the measured peak bond stress τ_{max} with the number of cycles (in a similar manner as in Fig. 10d) for two fibres located respectively at the side of the free surface (refer to fibre West) and in the inner side (fibre East). Degradation of bond stresses is consistently observed, in similar proportions as those of centric tests [8,35]. Moreover, for ties with eccentric bars, reduced bond stresses developed at the side of the free surface with respect to the inner sides of the bar. This can be explained by the potential spalling of concrete cover [41] for the faces close to the free surfaces leading to lower peak bond stresses as well as to more pronounced degradations with the number of cycles of the latter, see Fig. 13b.

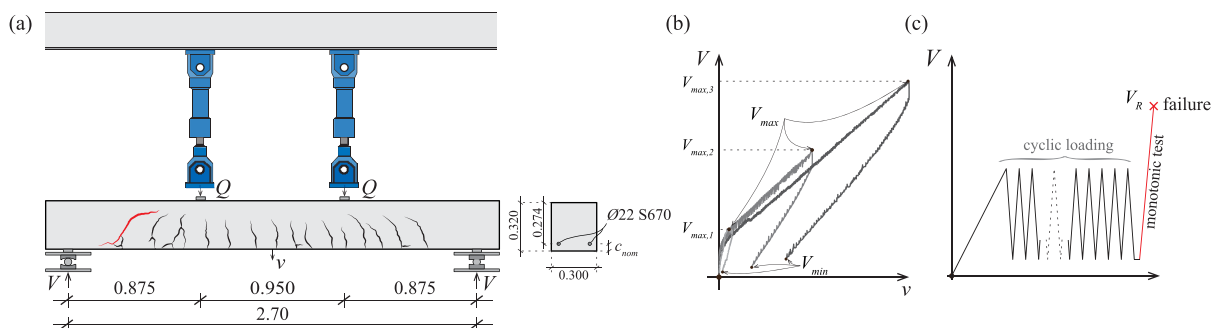


Fig. 14. Beam tests: (a) front view of test setup; (b) load levels selected for the cyclic loading; and (c) loading pattern (quasi-static cyclic loading + monotonic test until failure); (shear force V at supports including self-weight).

Table 3
Main parameters and measured shear strengths of beam tests.

	$V_{cycl,max}$ [kN]	$V_{cycl,min}$ [kN]	$R = V_{min}/V_{max}$	f_c [MPa]	V_R [kN]
SC75	27.8	5.27	0.19	33.3	95.4
SC76	54.0	7.25	0.13	36.0	97.1
SC77	86.4	10.2	0.12	36.6	80.7

5. Beam tests

5.1. Main parameters and test setup

Three four – point bending tests were performed on 3.0 m reinforced concrete beams with 0.30×0.32 m cross section, Fig. 14. The nominal effective depth was constant for all tests and equal to 274 mm. Two concentrated forces were introduced symmetrically by means of two hydraulic jacks with a total capacity of 1 MN. The jacks were fixed to an external steel frame and placed at a constant distance to the support equal to 875 mm, representing a shear span of $3.2d$. The beams were supported on two 50×300 mm steel plates which were arranged on two bearings allowing for free rotation and longitudinal displacements of the supports.

All beams were cast with normal strength concrete whose compressive strength at the testing day ranged between 33.2 and 36.6 MPa (average of three compressive tests on 160×320 mm concrete cylinders). The maximum aggregate size was 16 mm for all test specimens. The cement type was CEM II/B-M (T-LL) 42.5 N, in accordance with [23], with a water-to-cement ratio equal to 0.45.

The flexural reinforcement of all beams consisted of two high strength $\varnothing 22$ reinforcing bars (yield strength $f_y = 701$ MPa, $\rho = 0.92\%$)

and no compression reinforcement was provided. The nominal concrete cover c_{nom} was 35 mm. Additional details are given in Table 3. The concrete surface behaviour was tracked by means of digital image correlation. In addition, FOM sensors were glued (both on the top and bottom side) in one of the two bars forming the flexural reinforcement. All members were tested in displacement–control mode with a loading rate ranging between 0.01 and 0.05 mm/s (typical test duration of 15 min). Every member was first subjected to 50 quasi–static load cycles, then unloaded and reloaded until shear failure occurred on one side. Regarding the maximum force $V_{cycl,max}$ during cyclic action, three load levels were investigated with the three beams (see also Table 3):

- Beam SC75, load level I – $V_{cycl,max}$ corresponding to the flexural cracking development.
- Beam SC76, load level II – $V_{cycl,max}$ corresponding to $0.5 - 0.55V_R$ (where V_R refers to the ultimate failure load)
- Beam SC77, load level III – $V_{cycl,max}$ corresponding to the onset of the quasi – horizontal branch of the shear critical crack (refer to [42] for additional details).

The maximum shear force $V_{cycl,max}$ during cyclic loading corresponds to the shear force at supports.

5.2. Test results

The measured load – displacement curves (shear force V at support including the self–weight) are shown in Fig. 15 for the three members with three different load levels $V_{cycl,max}$. The vertical displacement is evaluated by means of a LVDT placed at the centre of the beam. In all specimens, an increase of vertical displacement was observed due to the

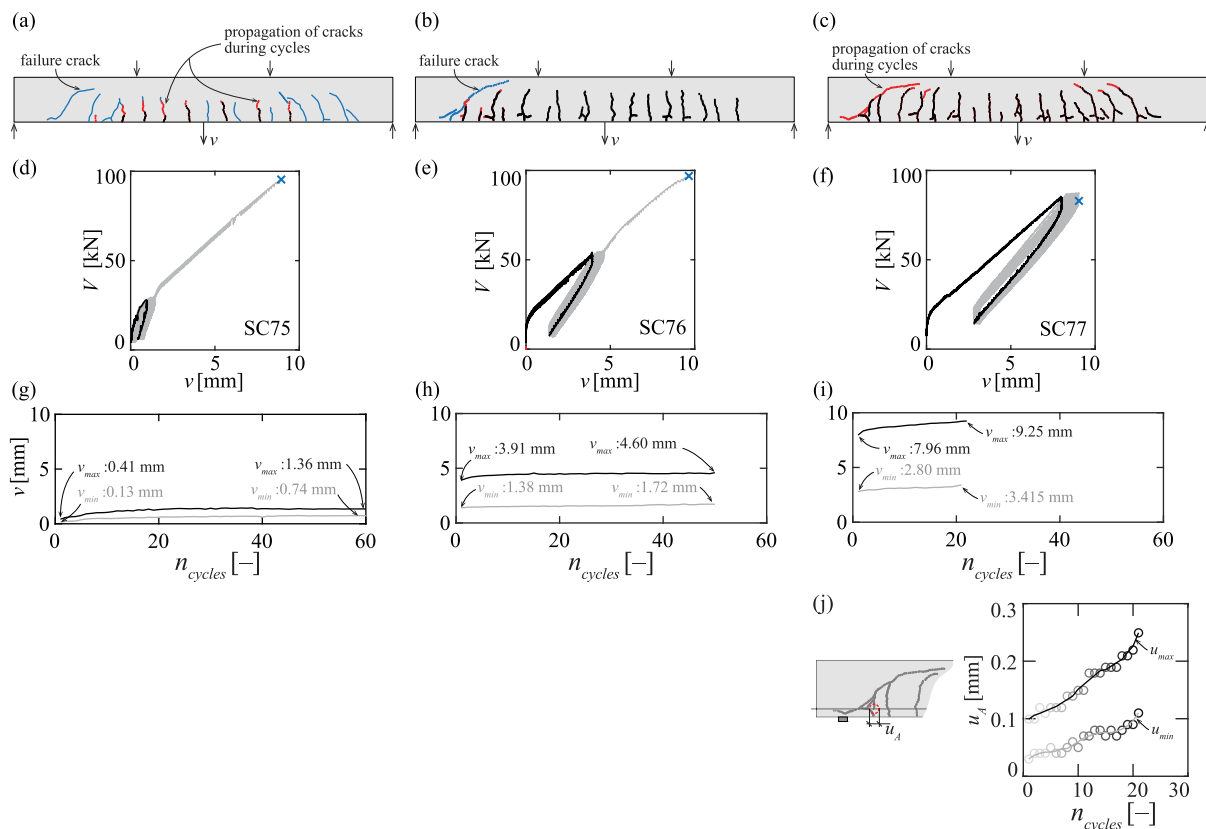


Fig. 15. Cracking pattern after first cycle (in black), propagation during cyclic loading (in red), at failure (in blue) for beams: (a) SC75; (b) SC76 and (c) SC77; load–displacement curves $V - v$ for beams (d) SC75; (e) SC76 and (f) SC77; maximum deflection developed during cyclic loading for beams (g) SC75; (h) SC76 and (i) SC77; and (j) development of horizontal component of crack opening u_A at the level of the flexural reinforcement with the number of cycles for the shear critical crack leading to the failure of member SC77.

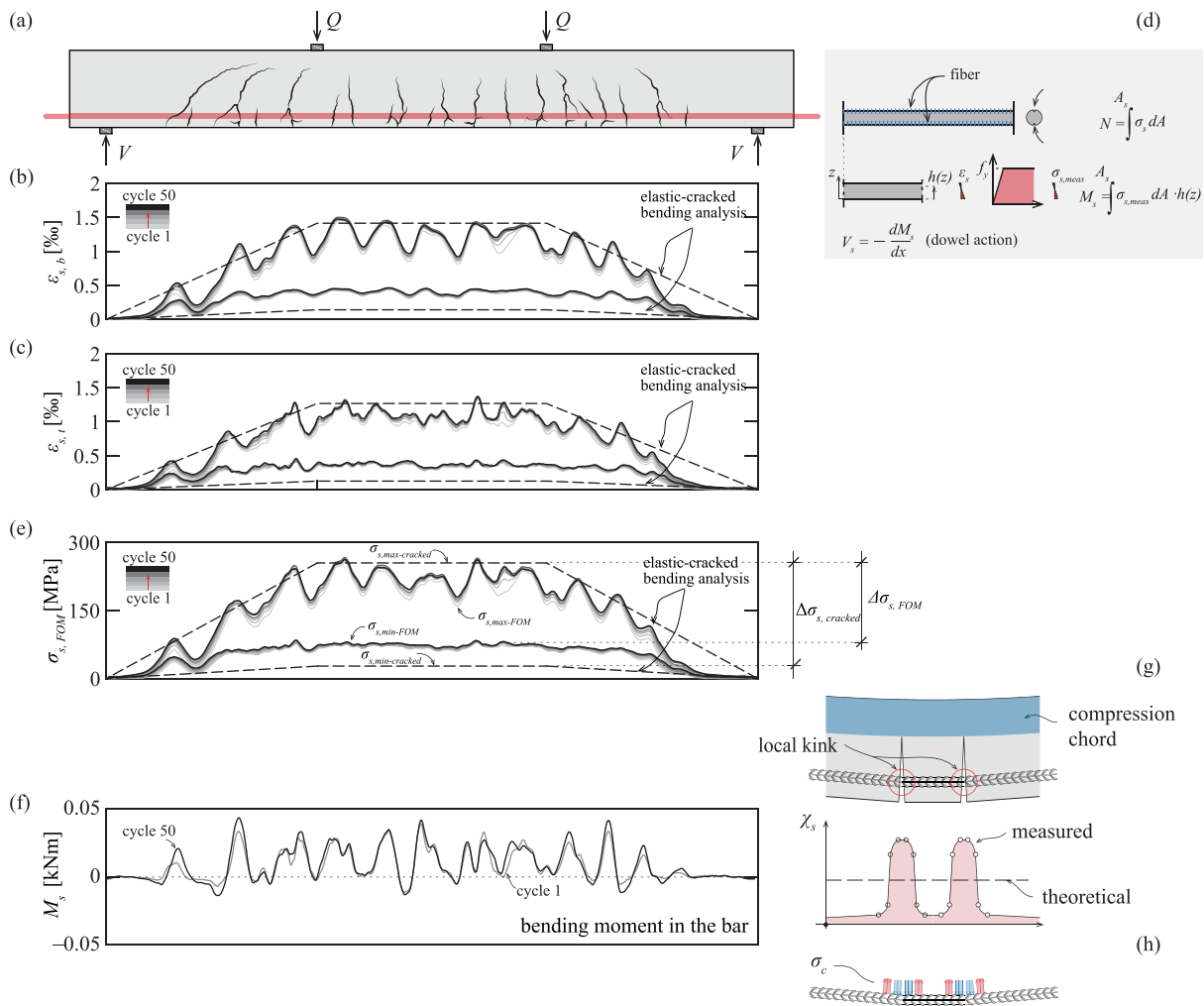


Fig. 16. Beam SC76 – (a) cracking pattern observed at failure; profiles at maximum and minimum load for selected cycles (refer to colour scale at top left side); (b) measured rebar strains $\epsilon_{s,b}$ at bottom side; (c) measured rebar strains $\epsilon_{s,t}$ at top side; (d) description of fibre position and approach for calculating rebar internal forces; (e) comparison between calculated average stresses $\sigma_{s,FOM}$ from FOM strains and steel stresses according to an elastic-cracked calculation $\sigma_{s,cracked}$; (f) bending moments in the reinforcing bar M_s ; (g) localized kinking of the bar in a cracked section with schematic representation of local increase of curvature χ_s ; and (h) local contact forces due to kinking of the bar.

effect of cyclic loading. For specimens SC75, SC76, this can be attributed to the cyclic response of concrete and to bond degradation. Larger residual crack openings also developed for increasing number of cycles as well as higher strains in rebars at maximum shear force $V_{cycl,max}$. No shear failure occurred in these two tests during the cycles.

For specimen SC77, the development of the quasi-horizontal shear crack during the loading cycles gave rise to a failure in shear at a maximum shear force $V_{cycl,max}$ equal to 84% of the reference shear failure load V_R (average of shear failure loads measured in specimens SC75 and SC76). Failure occurred by propagation of the critical shear crack.

Details on the evolution of the midspan displacement with the cycles are additionally shown in Figs. 15d-f obtained from LVDT and DIC readings. It can be noted a significant increase in the maximum deflection during the cycles (black curves in Figs. 15g-i, particularly during the first ones) as well as a residual deflection (light grey curves). To a large extent, these phenomena can be related to the imperfect closure of cracks lips, to the degradation of bond properties and to the development of negative tension-stiffening effects. As previously mentioned, beam SC77 was subjected to load cycles in which the maximum applied shear force corresponded to the formation of the quasi-horizontal branch of the critical shear crack. During the cyclic process, the member failed in shear due to propagation of the crack tip towards the load introduction plate, Fig. 15c. This development was accompanied by the

evolution of the horizontal crack opening u_A at the level of the flexural reinforcement, see Fig. 15j (black curves for maximum horizontal crack opening and light grey curves for residual crack opening).

In addition to DIC, FOM sensors were installed in the top and bottom surfaces of steel rebars. The strains were evaluated with a spatial resolution of 0.65 mm and the raw results were smoothed over an average length equal to two times the bar diameter (as for tests on ties, according to the disturbed region observed in pull-out tests).

Figs. 16b-c show the FOM results for all cycles with respect to the top and bottom rebar surface (values at maximum and minimum applied shear forces $V_{cycl,max}$ and $V_{cycl,min}$). In the beam region with constant bending moment, it can be noted a difference between top and bottom rebar strain at each section. In particular, the bottom strain results consistently higher than top rebar strain. This can be explained by the curvature of the rebar as already stated by Ritter [1] (refer to Fig. 1a), an aspect usually neglected for design. Such response is however not observed in other regions, namely in regions subjected to a combination of bending and shear. For these regions, the effect of inclined shear cracks allows for activation of dowelling forces, thus leading to relatively high and concentrated curvatures at the opposite sides of an inclined crack (double-hinge mechanism) dominating the difference between top and bottom bar strains.

On this basis, by assuming plane sections of the bar to remain plane

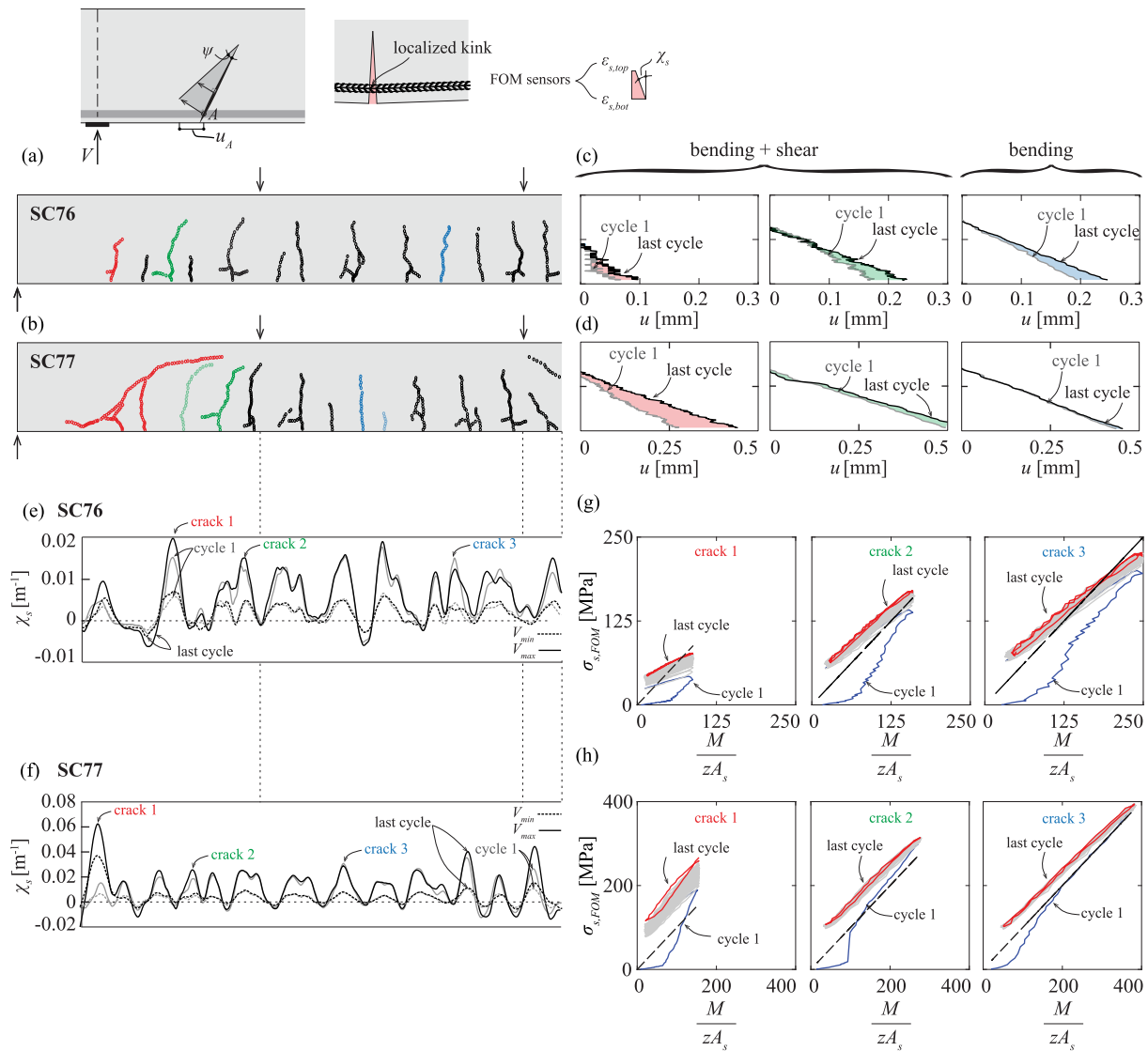


Fig. 17. Cracking pattern observed with DIC during cyclic loading for beams (a) SC76 and (b) SC77; evolution of horizontal crack opening u between first (grey lines) and last (black lines) load cycle for three selected cracks (refer to red, green and blue cracks) for beams (c) SC76 and (d) SC77; profiles of measured rebar curvatures between first (grey lines) and last (black lines) load cycles at the maximum rebar stress N_{max}/A_s (continuous lines) and minimum rebar stress N_{min}/A_s (dashed lines) for specimens (e) SC76 and (f) SC77; and $\sigma_{s,FOM} - M/zA_s$ behaviour during cyclic loading for three selected cracks in the region with combined bending and shear actions (red and green cracks) or with just bending actions (blue cracks) for specimens (g) SC76 and (h) SC77. (For interpretation of the references to color in this figure legend, the reader is referred to the web version of this article.)

and an elastic–plastic behaviour of the steel, the normal forces and bending moments in the bar can be determined by integration of the cross–sectional stresses, see Fig. 16d. The profiles of average rebar stresses $\sigma_{s,FOM}$ are shown in Fig. 16e. The measured values are also compared with the theoretical stresses resulting from beam analysis considering cracked conditions (lever arm $z = d - c/3$ where c is the height of the compression zone calculated assuming elastic behaviour of the compression zone and neglecting tension–stiffening). It can be noted that the calculated values locally underestimate the measured stresses at the maximum load $V_{cycl,max}$, in particular in regions with inclined shear cracking. This phenomenon has been consistently observed in such members [13] and can be explained by the development of inclined shear cracks [43] (according to the shift of bending moments). On the other hand, at minimum shear forces $V_{cycl,min}$, the analytical values largely underestimate the average measured rebar stresses. In particular, the measured stress variations in the rebar during cycles attain values (≈ 180 MPa) which are 30% lower than the calculated stress variations for a fully–cracked response (≈ 250 MPa). It can be noted that this lower

variation of stresses have favourable implications on the potential fatigue response of reinforcement.

Moreover, the marked localization of bar bending clearly stems out in Fig. 16f (resulting from the shift on the position of the waves of the strain profile along the longitudinal direction, Fig. 16b–c), owing to the local kinking in the bar, Figs. 16g–h.

5.3. Interpretation of test results

As already noted by Ritter [1], the consideration of an average stress in the cross section of a bar is a simplification of its actual response, as a non–uniform profile of stresses in the longitudinal reinforcement develops due to the curvature of plane sections [1]. The reality is in fact even more complex, as once cracking occurs at a section, the steel bar is actually kinked with concentrated curvatures at the location of the cracks, see Fig. 16g. Kinking of the bar is thus associated to the activation of transverse forces at the location of cracks, whose local force distribution is outlined in Fig. 16h. As a consequence, transversal

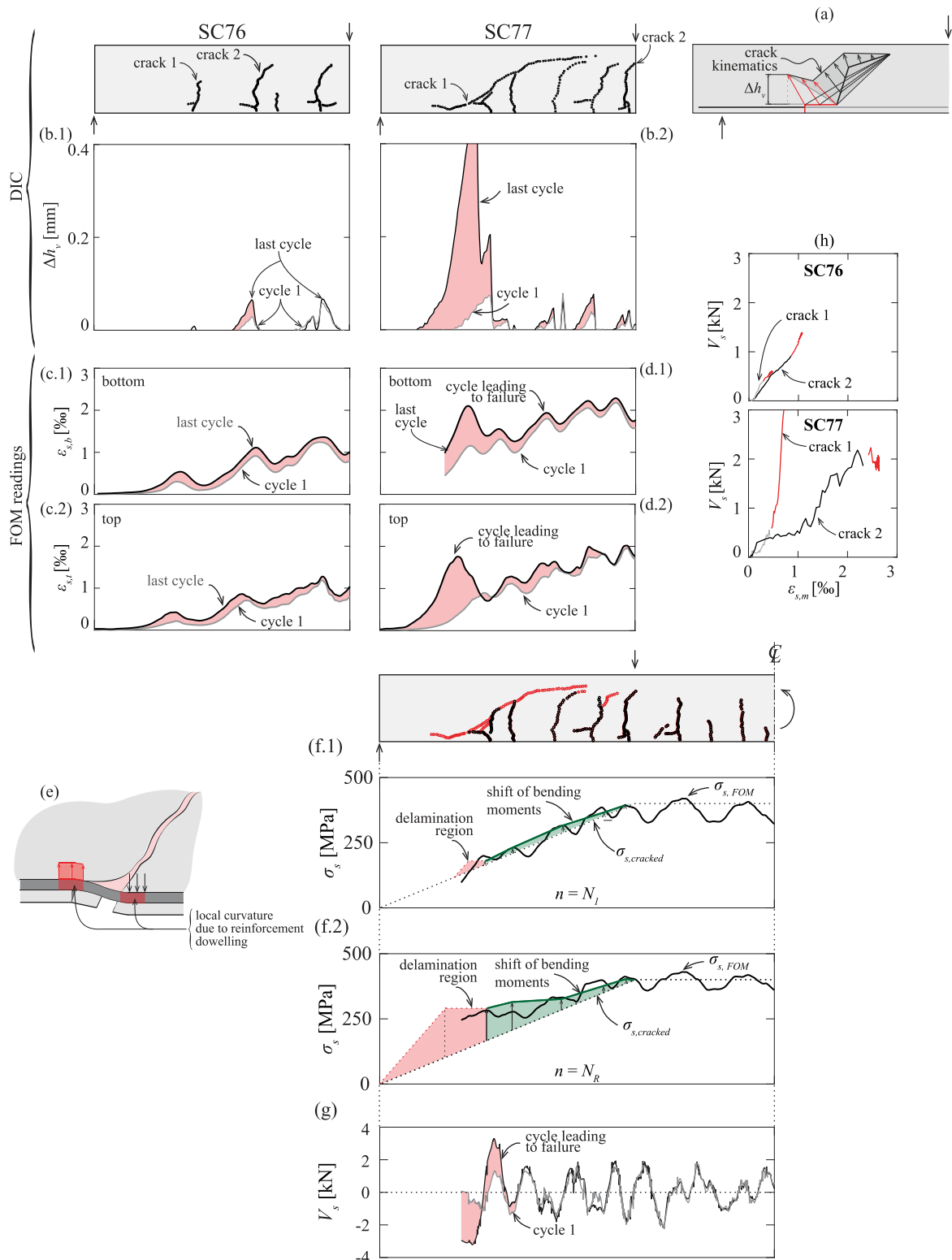


Fig. 18. (a) geometry of critical shear crack and delamination cracks [46]; vertical crack opening Δh_v , for beams (b.1) SC76 and (b.2) SC77; profiles of bottom and top strains at the maximum and minimum level of shear force for beams (c.1)-(c.2) SC76 and (d.1)-(d.2) SC77, respectively; (e) local curvature due to dowelling of reinforcement; stress at the level of the flexural reinforcement: comparison between measured stresses $\sigma_{s,FOM}$ and calculated stresses $\sigma_{s,cracked}$ in a bare bar according to an elastic-cracked analysis, for specimen SC77 after (f.1) the first cycle and (f.2) the cycle leading to failure $N = N_R$; (g) profile of dowelling forces during the first and last load cycle for specimen SC77; and (h) dowelling forces developing at the level of flexural reinforcement for two selected cracks (grey and black lines refer to dowelling force V_s developed in the first cycle, red curves are the peak dowelling forces at each cycle). (For interpretation of the references to color in this figure legend, the reader is referred to the web version of this article.)

compressive and tensile forces develop in the vicinity of the crack, being a potential source for longitudinal delamination cracks together with other phenomena (as bond splitting [44] stresses or spalling due to deviation forces [45]).

The effects of local kinking of the bar can be observed also in Fig. 17 for the region in pure bending (between loads, refer for instance to crack 3 in blue). The FOM readings show in this region low or no curvatures between cracks (due to the fact that the bar is embedded in uncracked concrete with limited deformation), but relatively high and concentrated curvatures at the location of the cracks. These effects can also be clearly appreciated in the region subjected to bending and shear (red and green cracks for instance in Fig. 17). In this region, flexural cracks develop in an inclined manner (Cavagnis et al. [10]) and their opening leads kinematically to the development of a delamination crack and dowelling of the reinforcement (refer to Fig. 2c). In this case, other than the peaks of positive strains at the location of the cracks, negative curvatures develop along and at the end of the delamination crack indicating the presence of bending associated to dowelling of the reinforcement (Fig. 2c). The horizontal component of the crack opening u over the height (Figs. 17c–d), obtained by means of DIC, reveals that in the region subjected to pure bending, the profile is almost linear. In addition, there is some moderate increment of the crack opening under cyclic loading, which can be attributed primarily to bond degradation (refer to Section 4.3). This phenomenon is however significantly more pronounced in the region subjected to bending and shear where inclined cracks develop (refer particularly to red crack in specimen SC77, Fig. 17d). This is justified, other than bond degradation, by the progression of the delamination crack and its associated increase of strains in the reinforcement, Cavagnis et al. [10,42] (refer to the behaviour in Figs. 17g–h in terms of measured steel stress $\sigma_{s,meas}$ – steel stress in the bar M/zA_s , according to an elastic–cracked calculation) and by the progression of the upper tip of the crack towards the loading plate (upper quasi–horizontal branch of the crack).

The progression of the delamination crack and the upper branch of the shear crack are further explained in Fig. 18. According to the kinematics of an inclined crack (Fig. 2c), a delamination crack develops due to dowel action of the reinforcement [42,46]. Such progression is shown in Fig. 18b with respect to the DIC readings, with the most inclined cracks leading to larger progressions. In the delaminating region, bond stresses are disabled or reduced. As a consequence, the average reinforcement strain increases significantly. This fact is clearly perceptible in specimen SC77 (corresponding to the most inclined and developed shear crack), with large increments of strains at the delamination region as the critical shear crack progresses with the number of cycles (Fig. 18d). Such increase of measured strains in the delamination region is in agreement to the theoretical considerations performed by Fernández Ruiz et al. [46] and require to be accounted for a suitable evaluation of the shear strength (refer to Fig. 18f).

In addition, other than the delamination crack, the shift of bending moments needs to be considered in order to properly evaluate the stress state close to failure at the level of the flexural reinforcement, [13] (see Figs. 18f–h). This was already acknowledged by Cavagnis et al. [13], which considered that all cracks tributary to the critical shear crack give rise to a rather linear profile of the horizontal component of the crack width u (which is in fact proportional to the bending moment at the crack tip). This fact is clearly visible from the shift of the steel stress behaviour presented in Figs. 17g–h in terms of local steel stresses $\sigma_{s,FOM}$ with respect to M/zA_s (where M is the acting bending moment, $z = d - c/3$ is the lever arm according to an elastic–cracked analysis and A_s is the area of flexural reinforcement).

The propagation of the shear crack with the number of cycles was particularly observed in specimen SC77 failing during the loading cycles. For this specimen, the critical shear crack progressed both with respect to its upper quasi–horizontal branch and to the development of the delamination crack (Figs. 18b,2.f.1) [47]. This progression was associated to an increase of the dowel action of the reinforcement

calculated on the basis of its strains (Figs. 18g–h). It can be noted that a consistent prediction of the failure load can be performed on the basis of the theoretical approach presented by Fernández Ruiz et al. [47], with an estimated failure load of 81.5 kN, closing matching the actual one of 80.7 kN (where the estimated failure load is calculated by considering a monotonic shear resistance $V_{R1} = 96.2$ kN – average of failure loads of specimens SC75 and SC76 – and failure after 22 cycles).

6. Conclusions

Recent advancements on measurement techniques allow for a notable step forward in the understanding of the actual response of embedded reinforcement and its interaction with concrete. In particular, the implementation of Fibre–Optical–Measurement systems (FOM) is allowing for high quality readings of the longitudinal strains in a rebar with low disturbance of the behaviour.

This paper revisits the interaction between reinforcement and concrete by performing tests on three different types of structural elements: pull–out tests, tension tests on ties subjected to cyclic loading and four–point bending tests under cyclic loading. A special attention is set on the response of potentially brittle phenomena (sensitive to stress concentrations and crack propagations), such as fatigue under cyclic loading or shear failures in beams without transverse reinforcement.

The main conclusions of this research are listed below:

Pull–out tests

- Strong strain (and stress) gradients are measured near to the ribs of bars, originated by local contact forces due to mechanical engagement.
- The observed strain gradients and high strain values observed in the rebars confirm that tension tests on bare rebars for the evaluation of the material strength under fatigue loading can be unsuitable to characterize the response of embedded reinforcement.

Tension tests

- The profile of measured strains in reinforced concrete ties confirmed the suitability of considering rigid–plastic bond laws as a rough but sound simplification.
- FOM measurements show the development of negative tension–stiffening effects during the unloading process. Bond degradation was tracked with the number of cycles providing results in sound agreement with reductions proposed in the literature (both for peak bond values τ_a and for negative values of the bond stress τ_i).
- Measured stress variations during unloading can significantly differ from values calculated on bare bars (which could be favourable for fatigue verification) due to a large extent by the imperfect closure of cracks.

Beam tests

- Local kinking of rebars was observed at bending (vertical) cracks due to compatibility of deformations. Such kinking originates local transverse tensile stresses in the concrete leading to the potential development of longitudinal delamination cracks and cover spalling.
- Lower stress variations due to bending were detected in the longitudinal reinforcement with respect to theoretical values calculated with elastic–cracked analyses due to imperfect closure of cracks and negative tension–stiffening effects. As for the reinforced concrete ties, this has favourable implications on the fatigue response of reinforced concrete members.
- Based on the recorded strain profiles and by derivation of the calculated bending moments in the longitudinal bars, FOM allows quantifying the dowel action at shear (inclined) cracks.
- The level of maximum shear force plays a significant role in the propagation of shear cracks leading to failure. Shear displacements

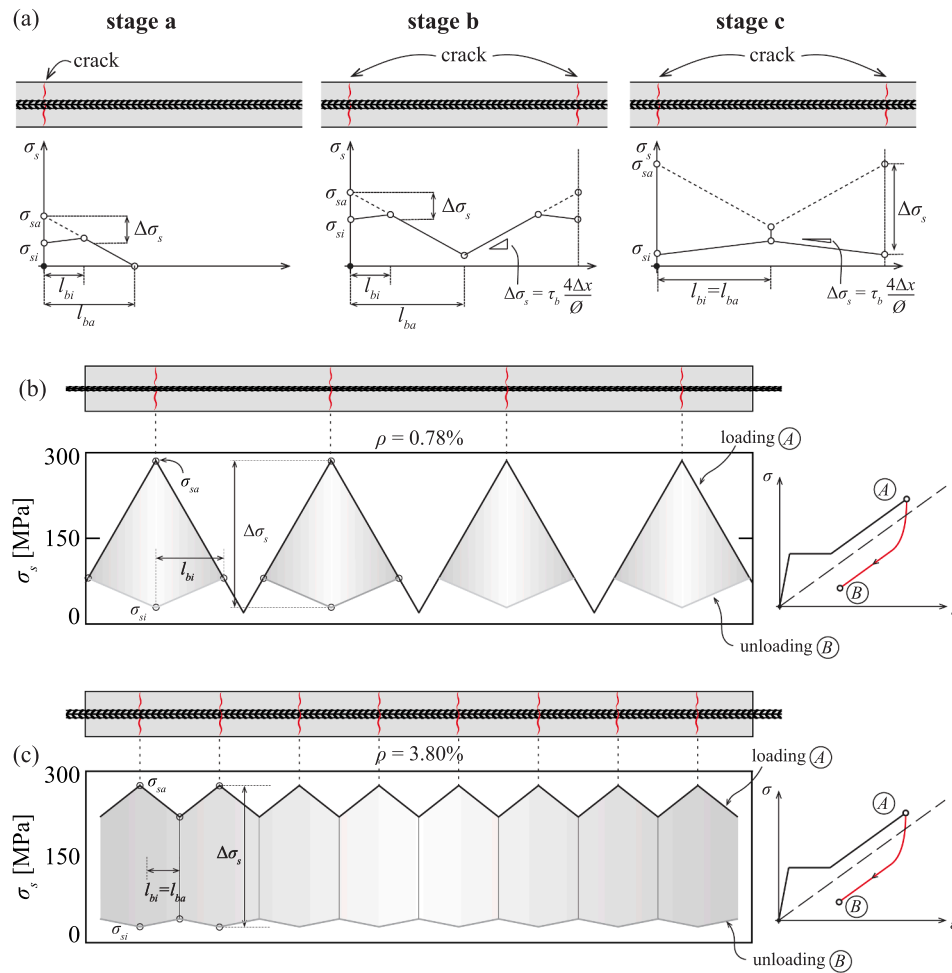


Fig. A.19. Negative tension–stiffening: (a) different unloading stages; comparison of steel stress distribution for two reinforced concrete ties with reinforcement ratios equal to (b) 0.78% and (c) 3.80% respectively – black lines refer to maximum steel stress (loading phase) while grey lines refer to minimum steel stress (unloading phase).

were observed in regions subjected to shear forces, thus leading to the formation of delamination cracks. Such cracks lead to a loss of the bond strength and to an increase of the opening of the critical shear crack. The development of the delamination crack is also associated to dowelling forces in the reinforcement (potentially detrimental for fatigue issues), but this effect is mostly noticeable when the specimen is near to its shear failure.

CRedit authorship contribution statement

Raffaele Cantone: Methodology, Software, Validation, Formal analysis, Investigation, Resources, Data curation, Writing - original draft, Writing - review & editing, Visualization. **Miguel Fernández Ruiz:** Conceptualization, Formal analysis, Writing - review & editing, Supervision, Project administration. **Aurelio Muttoni:**

Conceptualization, Writing - review & editing, Supervision, Project administration, Funding acquisition.

Declaration of Competing Interest

The authors declare that they have no known competing financial interests or personal relationships that could have appeared to influence the work reported in this paper.

Acknowledgements

The authors would like to gratefully acknowledge the support and funding of the Swiss Federal Road Authority, through the project AGB-2015-011.

Appendix A. Response of tension ties including its unloading response

This Appendix presents the model developed by Muttoni and Fernández Ruiz (2007) [32] to evaluate the response of tension ties including their unloading response. The formulas presented herein have been used for the evaluation of the analyses presented in this paper.

Regarding monotonic loading of a reinforced concrete member, once cracking occurs, the cross – sectional equilibrium of forces may be described in the following manner:

$$\sigma A = \sigma_s A_s + \sigma_c A_c \tag{A.1}$$

in which σ is the average stress in the tie, A the gross area, σ_s the steel stress and σ_c the concrete stress. If the tensile softening of concrete is neglected at the crack location, the average stress σ corresponds to $\sigma_{sa}\rho$, being ρ the reinforcement ratio and σ_{sa} the steel stress at the crack. Considering a rigid-plastic law for bond over the transfer length l_{ba} [29], from the equilibrium of forces it may be established the equation describing the longitudinal steel stress in the loading regime (refer to the dashed lines Fig. A.19a), as follows:

$$\sigma_{sa} \frac{\pi}{4} \phi^2 = \pi \phi l_{ba} \tau_a \quad (\text{A.2})$$

The maximum value of the transfer length $l_{ba,max}$ is derived by considering that at the end of the crack development phase the steel stress $\sigma_{sa} = \frac{f_{ct,eff}}{\rho}$:

$$l_{ba,max} = \frac{\phi f_{ct,eff}}{4\rho\tau_a} \quad (\text{A.3})$$

where $f_{ct,eff}$ is the effective concrete tensile strength.

Since the crack opening is the integration of the difference between steel and concrete strains along the concrete member, the crack width w after the loading process may be derived as:

$$w = \frac{\sigma_{sa}^2 \phi}{4E_s \tau_a} = \frac{\sigma^2 \phi}{4\rho^2 E_s \tau_a} \quad (\text{A.4})$$

So, considering the maximum transfer length $l_{ba,max}$, the crack opening in the stabilized cracking phase results:

$$w = \left(\frac{2\sigma_{sa}}{E_s} - \frac{f_{ct,eff}}{\rho E_s} \right) \frac{\phi f_{ct,eff}}{4\rho\tau_a} \quad (\text{A.5})$$

During the unloading process, Fig. 11b, the complex geometry of crack lips yields to residual crack openings. An estimate of these residual crack openings was performed by Hordijk [37,38] who derived empirically the stress necessary to reclose the crack as a function of the crack width. Thus, due to crack closure, concrete develops compressive stresses which cannot be neglected in the cross-sectional equilibrium, Fig. 11a.2. The average stress during unloading is then:

$$\sigma_{per} = \sigma_{si}\rho + \bar{\sigma}_c \quad (\text{A.6})$$

considering that the stress is $\Delta\sigma = \Delta\sigma_s\rho - \bar{\sigma}_c$, with $\bar{\sigma}_c$ according to [37], Fig. 11d.

$$\bar{\sigma}_c = f_{ct,eff} \left(0.004 \left(\log \left[\frac{w}{w_c} \right] \right)^5 - 0.16 \sqrt{1 - \frac{w}{w_c}} \right) \quad (\text{A.7})$$

As shown in [32], the crack width during the unloading process w_{per} needs to be calculated in a different manner as a function of the regime (cracking process/ stabilized cracking) in which unloading is performed, Fig. 11b:

- **Stage a** – unloading in the crack development stage

$$w_{per} = \left[(\sigma_{per} + \Delta\sigma)^2 - (\Delta\sigma + \bar{\sigma}_c)^2 \frac{\tau_a}{\tau_a + \tau_i} \right] \frac{\phi}{4\rho^2 E_s \tau_a} \quad (\text{A.8})$$

- **Stage b** – Unloading in the stabilized cracking: $l_{bi} < l_{ba,max}$

$$w_{per} = \left[2(\sigma_{per} + \Delta\sigma) - f_{ct,eff} - \frac{(\Delta\sigma + \bar{\sigma}_c)^2}{f_{ct,eff}} \frac{\tau_a}{\tau_a + \tau_i} \right] \frac{\phi f_{ct,eff}}{4\rho^2 E_s \tau_a} \quad (\text{A.9})$$

- **Stage c** – Unloading in the stabilized cracking: $l_{bi} = l_{ba,max}$

$$w_{per} = \left[2(\sigma_{per} - \bar{\sigma}_c) + \frac{\tau_i f_{ct,eff}}{\tau_a} \right] \frac{\phi f_{ct,eff}}{4\rho^2 E_s \tau_a} \quad (\text{A.10})$$

Fig. A.19 presents, for instance, the results of this approach [32] for two concrete ties (same geometry of the tests in Section 4) with reinforcement ratios equal to 0.78% and 3.80% respectively (as for specimens TC04 and TC06). The results are provided both for loading and unloading stages (a target ratio R equal to 0.1 and a maximum rebar stress equal to 275 MPa is imposed in accordance with loading rates of the tests). The results show that crack spacing is largely governed by reinforcement ratio and the specimen with ρ equal to 0.78% remains in stage b after unloading while the specimen with ρ equal to 3.80% reaches stage c of the behaviour, Fig. A.19a.

References

- [1] Ritter W. Die Bauweise Hennebique. *Schweizerische Bauzeitung* 1899;6(33/34): 49–52.
- [2] *fib Bulletin* 10, Bond of reinforcement in concrete. 2000.
- [3] Gambarova PG, Plizzari G, Rosati G. Bond mechanics including pull-out and splitting failures. *FIB Bulletin 10: Bond of Reinforcement in Concrete* 2000.
- [4] Goto Y, Otsuka K. Internal cracks formed in concrete around deformed tension bars. *ACI J Proc* 1971;68(4):244–51.
- [5] Fernández Ruiz M, Muttoni A, Gambarova PG. Analytical modeling of the pre- and post - yield behavior of bond in reinforced concrete. *J Struct Eng* 2007;133(10): 1–27.
- [6] Valeri P, Fernández Ruiz M, Muttoni A. Experimental research on textile reinforced concrete for the development of design tools. In: Proceedings of the 12th fib International PhD Symposium in Civil Engineering, (Prague, Czech Republic); 2018. p. 169–76.
- [7] Gómez Navarro M, Lebet JP. Concrete cracking in composite bridges: Tests, models and design proposals. *Struct Eng Int J Int Assoc Bridge Struct Eng (IABSE)* 2001;11 (3):184–90.
- [8] Balázs G. Fatigue of Bond. *ACI Mater J* 1991;88(6):620–9.
- [9] *Correlated Solutions, Vic-3D 2010, Reference Manual*; 2010.
- [10] Cavagnis F, Fernández Ruiz M, Muttoni A. Shear failures in reinforced concrete members without transverse reinforcement: An analysis of the critical shear crack development on the basis of test results. *Eng Struct* 2015;103:157–73.
- [11] Cavagnis F, Fernández Ruiz M, Muttoni A. An analysis of the shear-transfer actions in reinforced concrete members without transverse reinforcement based on refined experimental measurements. *Struct Concr* 2017;19(1):49–64.
- [12] Fernández Ruiz M, Muttoni A. Size effect in shear and punching shear failures of concrete members without transverse reinforcement: Differences between statically determinate members and redundant structures. *Struct Concr* 2018;19 (1):65–75.
- [13] Cavagnis F, Fernández Ruiz M, Muttoni A. A mechanical model for failures in shear of members without transverse reinforcement based on development of a critical shear crack. *Eng Struct* 2018;300–15.
- [14] Luna Technologies Inc., *Optical Backscatter Reflectometer 4600 User Guide*. Blacksburg, VA: Luna Technologies; 2013.
- [15] Hoult NA, Ekim O, Regier R. Damage/deterioration detection for steel structures using distributed fibre optic strains sensors. *J Eng Mech* 2014;140(12):1–9.
- [16] Regier R, Hoult NA. Concrete deterioration detection using distributed sensors. *Proc Inst Civ Eng Struct Build* 2015;168(2):118–26.
- [17] Davis MB, Hoult NA, Bajaj S, Bentz EC. Distributed sensing for shrinkage and tension-stiffening measurement. *ACI Struct J* 2017;114(3):753–64.
- [18] Barrias A, Casas JR, Villalba S. Embedded distributed optical fiber sensors in reinforced concrete structures—a case study. *Sensors* 2018;18(4).
- [19] Poldon JJ, Hoult NA, Bentz EC. Distributed sensing in large reinforced concrete shear test. *ACI Struct J* 2019;116(5):235–45.
- [20] Brault A, Hoult NA. Distributed reinforcement strains: measurement and application. *ACI Struct J* 2019;116(4).
- [21] Broth Z, Hoult NA. Dynamic distributed strain sensing to assess reinforced concrete behaviour. *Eng Struct* 2020;204:110036.
- [22] Lu X. Coherent Rayleigh time domain reflectometry: novel applications for optical fibre sensing [PhD thesis]. École Polytechnique Fédérale de Lausanne; 2016.
- [23] EN 197-1:2011. Cement - Part 1: Composition, specifications and conformity criteria for common cements; 2011.
- [24] EN1992-1-1:2004. Design of Concrete Structures - Part 1: General Rules and Rules for Buildings. Brussels, Belgium; 2004.
- [25] Moccia F, Kubski X, Fernández Ruiz M, Muttoni A. The influence of casting position and disturbance induced by reinforcement on the structural concrete strength. *Struct Concr* 2020;1:28.
- [26] Tilly GP. Fatigue of steel reinforcement bars in concrete: a review. *Fatigue Fract Eng Mater Struct* 1979;2(3):251–68.
- [27] Farra B, Jaccoud J-P. Influence of concrete and reinforcement on cracking of concrete structures, tech. rep. Test Rep. of Short-Term Imposed Strains on Ties, IBAP, Pub. 140. Lausanne (Switzerland): École Polytechnique Fédérale de Lausanne; 1993.
- [28] ISO 6892-1:2019. Metallic materials – Tensile testing – Part 1: Method of test at room temperature, vol. 1, no. 112; 2019. p. 70.
- [29] Marti P, Alvarez M, Kaufmann W, Sigrist V. Tension chord model for structural concrete. *Struct Eng Int* 1998;8(4):287–98.
- [30] Alvarez M. Influence of bond behaviour in the deformation capacity of reinforced concrete [PhD thesis]. Switzerland: ETH Zurich; 1998.
- [31] Kenel A. Biegetragverhalten und Mindestbewehrung von Stahlbetonbauteilen [PhD thesis]. Switzerland: ETH Zurich; 2002.
- [32] Muttoni A, Fernández Ruiz M. Concrete cracking in tension members and application to deck slabs of bridges. *J Bridge Eng* 2007;12(5):646–53.
- [33] Zanuy C, de la Fuente P, Albajar L. Estimation of parameters defining negative tension stiffening. *Eng Struct* 2010;32(10):3355–62.
- [34] Zanuy C. Investigating the negative tension stiffening effect of reinforced concrete. *Struct Eng Mech* 2010;34(2):189–211.
- [35] Tassios TP, Yannopoulos PJ. Analytical studies on reinforced concrete members under cyclic loading based on bond stress-slip relationships. *J Am Concr Inst* 1981; 78(3):206–16.
- [36] Cornelissen HA, Reinhardt HW. Uniaxial tensile fatigue failure of concrete under constant-amplitude and programme loading. *Mag Concr Res* 1984;36(129): 216–26.
- [37] Hordijk D. Local approach to fatigue of concrete [PhD thesis]. Technische Universiteit Delft; 1991.
- [38] Hordijk D. Tensile and tensile fatigue behaviour of concrete; experiments, modelling and analyses. *Heron* 1992;37(1):1–79.
- [39] Giuriani E. Experimental investigation on bond-slip law of deformed bars in concrete. In: *IABSE Colloquium, (Delft, Netherlands)*; 1981. p. 121–42.
- [40] Balázs G. Cracking analysis based on slip and bond stresses. *ACI Mater J* 1993;90 (4):340–8.
- [41] Brantschen F, Faria D, Fernández Ruiz M, Muttoni A. Bond behaviour of straight, hooked, U-shaped and headed bars in cracked concrete. *Struct Concr* 2016;17(5): 799–810.
- [42] Cavagnis F. Shear in reinforced concrete without transverse reinforcement: from refined experimental measurements to mechanical models [PhD thesis]. EPFL - École polytechnique fédérale de Lausanne; 2017.
- [43] Fernández Ruiz M, Muttoni A, Sagaseta J. Shear strength of concrete members without transverse reinforcement: A mechanical approach to consistently account for size and strain effects. *Eng Struct* 2015;99:360–72.
- [44] Tepfers R. A Theory of Bond Applied to Overlapped Tensile Reinforcement Splices for Deformed Bars. Chalmers University, P-73:2. Division of Concrete structures; 1973. p. 328.
- [45] Fernández Ruiz M, Plumey S, Muttoni A. Interaction between bond and deviation forces in spalling failures of arch-shaped members without transverse reinforcement. *ACI Struct J* 2011;107(3):346–54.
- [46] Fernández Ruiz M, Muttoni A, Sagaseta J. Shear strength of concrete members without transverse reinforcement: A mechanical approach to consistently account for size and strain effects. *Eng Struct* 2015;99:360–72.
- [47] Fernández Ruiz M, Zanuy C, Natário F, Gallego J, Albajar L, Muttoni A. Influence of fatigue loading in shear failures of reinforced concrete members without transverse reinforcement. *J Adv Concr Technol* 2015;13(5):263–74.